DESIGN OF A COLLIMATOR FOR BREAST-SPECIFIC GAMMA IMAGING AND ASSESSMENT OF NEC RATE FOR A PET SCANNER USING MONTE CARLO SIMULATIONS AND RESPONSE SURFACE METHODOLOGY

by

Didar Talat

B.S., Physics, Boğaziçi University, 2005

M.S., Institute of Biomedical Engineering, Boğaziçi University, 2007

Submitted to the Institute of Biomedical Engineering

in partial fulfillment of the requirements

for the degree of

Doctor

of

Philosophy

Boğaziçi University

2016

DESIGN OF A COLLIMATOR FOR BREAST-SPECIFIC GAMMA IMAGING AND ASSESSMENT OF NEC RATE FOR A PET SCANNER USING MONTE CARLO SIMULATIONS AND RESPONSE SURFACE METHODOLOGY

APPROVED BY:

Assoc. Prof. Dr. Albert Güveniş (Thesis Advisor)	.....
Prof. Dr. Yekta Ülgen	.....
Prof. Dr. Mehmed Özkan	.....
Assoc. Prof. Dr. Burak Güçlü	.....
Prof. Dr. İlhami Uslu	.....

DATE OF APPROVAL: 17 December 2015

In memory of my beloved ones, Mustafa, Tülün, Havva and Talat, who would have been so delighted to see me graduating. They will always be missed...

ACKNOWLEDGMENTS

Working on PhD has been not only a wonderful, but also a overwhelming process. In any case, I am thankful to many people for turning these long years into an unforgettable experience for me.

First, I would like to express my special appreciation to my advisor, Assoc. Prof. Albert Güveniş for supporting and guiding me to complete this study.

My special words of thanks should also go to my committee members Prof. Dr. Yekta Ülgen and Prof. Dr. Mehmed Özkan for their time and scientific advices.

I am indebted to Assoc. Prof. Dr. Burak Güçlü for reviewing my paper and providing me invaluable guidance.

I have been very privileged to be among such great company at Boğaziçi University. I would like to express my heart-felt gratitude to all my beloved friends Ahu Türkoğlu, Ayşe Sena Kabaş Sarp, Bige Vardar, Cemile Gezer, Deniz Nevşehirli, Fatma Gülden Temiz Şimşek, Filiz Ateş, Hakan Solmaz, İsmail Devecioğlu, Kazım Çamlıbel, Mehmet Kocatürk, Meltem Sevgi, Moataz Assem, Murat Tümer, Mustafa Kemal Ruhi, Müge Özker, Neslihan Sarıca, Özgür Kaya, Tuğba Köker and Uluç Pamuk. I specifically want to acknowledge my friend Bora Büyüksaraç. I am so much grateful for his sincere friendship and also for the help he provided to me. I learnt a lot from him. In addition, I would like to thank Burcu Tunç Çamlıbel, Esin Karahan Şenvardar, Gamze Bölükbaşı Ateş and Nermin Topaloğlu Avşar in particular for being in my life. I feel so lucky to have them by my side. I am deeply sorry that Mehmet Susam left us so early. He will never be forgotten.

I would like to extend my sincere word of thanks to Ayşegül Ünal and Çiğdem Günsür Çelik, for easing the administrative processes and of course to Muhammed

Avşar, who additionally became a very precious friend of mine.

I also would like to thank Arzu Onar, Banu Doralp Dinçer, Eren Büyükkapancı, Erman Önal, Nilay Çerçioğlu Büyükkapancı, Pırıl Sahil Tekin and Yıldız Özlem Ateş, who always fill my heart with joy as if we are still little kids. I am so fortunate to have them in my life.

None of these would have been possible without the constant support of my family. I would like to thank my mother Merih Talat, my father Zübeyr Talat and my sister Didem Talat for always believing in me. Without them I could never carry the weight of doing a PhD. I love them from the deepest of my heart. I also warmly appreciate the encouragement of my extended family.

Finally, I would like to thank researchers at Memorial Sloan Kettering Cancer Center, Dr. Assen Kirov for sharing the PET scanner model and Dr. Ross Schmidtlein for helpful contributions and valuable exchange on information about the digitizer modeling of the scanner.

The numerical calculations reported in the PET simulation study presented in this thesis were fully performed at TUBITAK ULAKBIM, High Performance and Grid Computing Center (TRUBA resources).

ACADEMIC ETHICS AND INTEGRITY STATEMENT

I, Didar Talat, hereby certify that I am aware of the Academic Ethics and Integrity Policy issued by the Council of Higher Education (YÖK) and I fully acknowledge all the consequences due to its violation by plagiarism or any other way.

Name :

Signature:

Date:

ABSTRACT

DESIGN OF A COLLIMATOR FOR BREAST-SPECIFIC GAMMA IMAGING AND ASSESSMENT OF NEC RATE FOR A PET SCANNER USING MONTE CARLO SIMULATIONS AND RESPONSE SURFACE METHODOLOGY

This thesis is composed of two studies that demonstrate the implementation of Monte Carlo (MC) simulations and response surface methodology (RSM) to specific problems in planar and tomographic nuclear medicine imaging.

In the first study, the collimator of a planar small field-of-view continuous crystal breast specific gamma camera is optimized by maximizing the lesion contrast-to-noise ratio (CNR) with respect to hole diameter, septal thickness and hole length. This study demonstrated that the pairwise interaction effects of the collimator parameters play a key role in determining the set of optimal parameter. As a result of optimization, a considerable improvement of up to 73% in CNR with respect to the reference collimators is achieved. Moreover, the critical region for detectability shifted towards the direction of smaller lesion diameter and lower tumor-to-background ratio. Another conclusion of the study is that the optimizer adapts itself to the spatial resolution/sensitivity trade-off as the lesion depth changes. Based on these findings, we conclude that the advantages obtained with this approach may lead to an advancement in collimator design.

Whereas, the second study is involved with the positron emission tomography (PET) camera performance based on the noise-equivalent-count rate (NECR). In this part, the effect of lower energy threshold (LET) and coincidence time window (CTW) on NECR is investigated over a range of activities. Our findings showed that both LET and CTW showed significant linear and quadratic effects. Moreover, the evidence of presence of interaction among parameters makes this approach superior in comparison to conventional one-variable-at-a-time assessment techniques. Through an in-depth

literature review, the proposed approach is also shown to be useful for a range of cameras for both human and animal use, as well as organ-specific and time-of-flight PET scanners.

Keywords: Collimator, contrast-to-noise ratio, Monte Carlo simulation, noise-equivalent-count rate, optimization, positron emission tomography, response surface methodology, scintimammography.

ÖZET

MONTE CARLO BENZETİMLERİ VE TEPKİ YÜZEY METODU KULLANILARAK MEME-SPESİFİK GAMA GÖRÜNTÜLEME İÇİN KOLİMATÖR TASARIMI VE BİR PET TARAYICI İÇİN NEC HIZI DEĞERLENDİRMESİ

Bu tez, Monte Carlo benzetimleri ve tepki yüzey metodunun planar ve tomografik nükleer tıp görüntüleme için spesifik problemlere uygulanmasını gösteren iki çalışmadan oluşmaktadır.

İlk çalışmada, planar küçük görüntü alanlı sürekli kristalli bir meme-spesifik gama kameranın kolimatörü kontrast-gürültü oranı (CNR) hol genişliği, septa kalınlığı ve hol uzunluğuna göre enbüyütülerek eniyilenmiştir. Bu çalışma, parametrelerin ikili etkileşimlerinin optimal kolimatörü hesaplamada kilit rol oynadığını göstermiştir. Eniyilemenin sonucu olarak, referans kolimatörlere göre CNR'de %73'e varan önemli bir artış elde edilmiştir. Ayrıca, saptanabilirlik açısından kritik olan bölge daha küçük lezyon ve daha düşük tümör-arka alan-oranı yönüne kaymıştır. Bu çalışmanın diğer bir sonucu olarak, lezyon derinliği arttıkça eniyileyicinin uzaysal çözünürlük/hassasiyet ödünleşimine adapte olduğu görülmüştür. Bu bulgular gözönünde bulundurularak, bu yaklaşımın kolimatör tasarımında bir gelişme sağlayabileceği öngörülmektedir.

İkinci çalışma ise gürültü-eşdeğeri-sayım hızı (NECR) ile değerlendirilen pozitron emisyon tomografisi (PET) performansı ile ilgilidir. Bu bölümde, geniş bir aktivite aralığı için düşük enerji eşiği (LTE) ile çakışma zaman penceresinin (ÇZP) NECR üzerindeki etkisi araştırılmıştır. Bulgularımız göstermiştir ki, DEE ve ÇZP anlamlı doğrusal ve ikinci derece etkilere sahiptir. Ayrıca, parametre etkileşimlerinin olduğuna dair kanıtlar, önerilen yöntemi her seferinde bir değişkenin etkisinin incelendiği konvansiyonel yöntemlere göre daha üstün kılmaktadır. Derinlikli bir literatür taraması, bu yaklaşımın insan ve hayvan kameraları, hatta organa özel ve uçuş-zamanı teknolojili (TOF) PET cihazları için de yararlı olduğunu göstermiştir.

Anahtar Sözcükler: Eniyileme, gürültü-eşdeğeri-sayım hızı, kolimatör, kontrast-gürültü-oranı, Monte Carlo benzetimi, pozitron emisyon tomografisi, sintimamografi, tepki yüzey metodu.

TABLE OF CONTENTS

ACKNOWLEDGMENTS iv
ACADEMIC ETHICS AND INTEGRITY STATEMENT vi
ABSTRACT vii
ÖZET ix
LIST OF FIGURES xiv
LIST OF TABLES xvi
LIST OF SYMBOLS xvii
LIST OF ABBREVIATIONS xix
1. MOTIVATION AND OBJECTIVES 1
2. DESIGN AND EVALUATION OF THE COLLIMATOR DIMENSIONS OF A BREAST-SPECIFIC SMALL FIELD-OF-VIEW GAMMA CAMERA USING MONTE CARLO SIMULATIONS AND RESPONSE SURFACE METHODOLOGY 3
2.1 Introduction 3
2.2 Background 4
2.2.1 Data and Image Quality in Scintillation Camera 4
2.2.1.1 Spatial resolution 4
2.2.1.2 Sensitivity 4
2.2.1.3 Energy resolution 5
2.2.2 Collimators 5
2.2.3 Overview: Breast-Specific Gamma-Imaging (BSGI) 8
2.2.4 Overview: Collimator Optimization Studies for Breast Imaging . 10
2.3 Materials and Methods 11
2.3.1 Design of a Breast-Specific Small Field-of-View Gamma Camera in SIMIND 11
2.3.2 Breast Scintigraphy Simulations 12
2.3.3 Calculation of the System Response 14
2.3.4 Implementation of RSM on Breast Scintigraphy Collimator Design Optimization 15

2.3.5 Performance Assessment of Collimators 19
2.4 Results 21
2.4.1 Validation of the Gamma Camera System 21
2.4.2 Second-Order Response Surface Model 22
2.4.3 Optimal Collimator Parameters 26
2.5 Discussion and Conclusion 32
3. ASSESSMENT OF NEC RATE FOR A PET SCANNER USING MONTE CARLO SIMULATIONS AND RESPONSE SURFACE METHODOLOGY . 37
3.1 Introduction 37
3.2 Background 38
3.2.1 Coincidence Detection in PET Imaging 38
3.2.2 Overview: Data Acquisition and Event Processing Parameters Affecting Statistical Data Quality 40
3.2.3 Relation between NECR and SNR 41
3.3 Materials and Methods 42
3.3.1 Model Description of the PET Scanner in GATE 42
3.3.2 Cluster Implementation of Simulations 44
3.3.3 Evaluation of the Scatter Fraction and the Noise-Equivalent-Count Rate and Validation of the Scanner 45
3.3.4 Implementation of the Response Surface Methodology 45
3.4 Results 47
3.4.1 Validation of Count Rate Simulations 47
3.4.2 Assessment of the Effect of Data Acquisition and Event Processing Parameters on Statistical Data Quality 48
3.5 Discussion and Conclusion 52
4. OVERALL CONCLUSIONS 56
APPENDIX A. Monte Carlo Tools in Nuclear Molecular Imaging 58
A.1 SIMIND 59
A.2 GATE (Geant4 Application for Tomographic Emission) 61
A.2.1 Simulation architecture 61
A.2.2 Parallelization of simulations 63
APPENDIX B. Principles of Response Surface Methodology 64

B.1 Sequential Workflow of RSM and Design of Experiments 64
B.2 Optimization of the Response 67
B.2.1 Analytical Approach 67
B.2.2 Numerical Approach 70
B.2.3 Robust Optimization 74
APPENDIX C. LIST OF PUBLICATIONS PRODUCED FROM THIS THESIS 75
REFERENCES 76

LIST OF FIGURES

Figure 2.1	Collimator types according to their geometries.	8
Figure 2.2	Geometry of a fan-beam collimator.	8
Figure 2.3	Side view, oblique view and bottom view of the camera and the breast phantom for a craniocaudal projection of the breast.	13
Figure 2.4	Cross-section of a parallel-hole collimator.	19
Figure 2.5	Spatial resolution vs. source-to-collimator distance for the camera.	22
Figure 2.6	Two factor interaction plots of collimator parameters.	25
Figure 2.7	Iso-desirability contours.	28
Figure 2.8	Iso-CNR plots with respect to TBR and lesion diameter for a lesion depth of 3 cm.	31
Figure 2.9	Collimators'performances at various lesion depths ranging from 1 cm to 5 cm for TBR values from 3:1 to 12:1.	32
Figure 3.1	True, scatter, random and multiple events detected in PET imaging.	39
Figure 3.2	2D and 3D data acquisition in PET.	41
Figure 3.3	Geometry of GE Discovery LS PET module modeled using GATE simulation platform.	43
Figure 3.4	Simulated 3D count rate response of GE Discovery LS PET module.	47
Figure 3.5	Box-Behnken design points shown in the 3D design space.	48
Figure 3.6	Predicted vs. simulated NECR.	49
Figure 3.7	Perturbation plot of scanning parameters for NECR.	51
Figure 3.8	Response surface plot of NECR with respect to scanning parameters.	52
Figure A.1	Interface of the CHANGE program.	60
Figure A.2	Simulation flags within the CHANGE program.	60
Figure B.1	Second-order experiment designs.	66
Figure B.2	Response surface of a second-order system displaying a maxium, a minimum and a saddle point.	69
Figure B.3	Simplex types.	70

Figure B.4 Update of the simplex (tetrahedron) in 3-parameter optimization case. 71

Figure B.5 Desirability functions according to weights for the maximization case. 73

Figure B.6 The transmitted variation in the response vs. the choice of level of a control factor. 74

LIST OF TABLES

Table 2.1	Comparison of $LaBr_3$:Ce crystal with other crystals used as scintillators in single photon gamma imaging.	12
Table 2.2	Range for the screening experiments.	15
Table 2.3	Initial guess of parameters and values near the optima observed at the final iteration of the gradient ascent.	15
Table 2.4	Two-level factorial design of experiments with center runs.	16
Table 2.5	Box-Behnken design of experiments with center runs.	18
Table 2.6	Levels of parameters for the Box-Behnken design.	19
Table 2.7	Experimental design for the Box-Behnken design in terms of actual factors and the corresponding CNR yield.	23
Table 2.8	Coefficients for the second-order models in terms of coded factors.	24
Table 2.9	ANOVA results for the quadratic response surface CNR model of the optimization case for lesion at 3 cm SCD.	26
Table 2.10	ANOVA results for the quadratic response surface CNR model of the optimization case for lesion at 5 cm SCD.	27
Table 2.11	Sensitivity, septal penetration and spatial resolution for optimum and other breast specific collimators at both 3 cm and 5 cm depths.	29
Table 2.12	Performance comparison of optimum and other breast specific collimators at both 3 cm and 5 cm depths.	29
Table 3.1	Design parameters and their experimental levels to model NECR.	46
Table 3.2	Box-Behnken design of experiments.	46
Table 3.3	ANOVA results for quadratic response surface model.	50

LIST OF SYMBOLS

A	Activity
Bq	Becquerel
Ci	Curie
d	Hole diameter of the collimator
D	Phantom diameter
eV	Electron Volt
f_{corr}	Average attanuation and deadtime correction factor
f_s	Scatter fraction
f_r	Random fraction
g_c	Geometric efficiency of a collimator
k	A constant that depends on the random estimation technique
K	A factor dependent on the type of filters used in image reconstruction
l	Hole length of the collimator
l_e	Effective hole length of the collimator
R	Rate of random coincidences
R_c	Collimator resolution
R_i	Intrinsic resolution of a gamma camera
R_s	System resolution of a gamma camera
s	Septal thickness of the collimator
S	Rate of scatter events
s_v	Image voxel size
T	Rate of true coincidences
T_t	Total true counts
$t_{1/2}$	Half-life
^{99m}Tc	Technetium-99 metastable
w	Minimum path length
Z_{eff}	Effective atomic number

α	Alpha particle
β^-	Electron
β^+	Positron
γ	Gamma photon
η	Number of gamma rays emitted per nuclear decay
λ	Eigenvalue
ε	Experimental error
μ	Linear attenuation coefficient
ω	Weight parameter
σ^2	Variance

LIST OF ABBREVIATIONS

2D	Two-dimensional
3D	Three-dimensional
ANOVA	Analysis of variance
BBD	Box-Behnken design
BGO	Bismuth germanate
BSGI	Breast-specific gamma imaging
CCD	Central composite design
CdTe	Cadmium telluride
CNR	Contrast-to-noise ratio
cpm	Counts per minute
cps	Counts per second
CPU	Central processing unit
CT	Computed tomography
CTW	Coincidence time window
CZT	CdZnTe - Cadmium zinc telluride
DoE	Design of experiments
DoI	Depth of interaction
EANM	European Association of Nuclear Medicine
FoV	Field-of-view
FWHM	Full-width at half-maximum
FWTM	Full-width at tenth-maximum
GP	General purpose
GSO	Gadolinium orthosilicate
HR	High resolution
HS	High sensitivity
$LaBr_3$:Ce	Cerium-doped lanthanum bromide
LET	Lower energy threshold
LGSO	Lutetium gadolinium oxyorthosilicate

LOR	Line-of-response
LSO	Lutetium oxyorthosilicate
LYSO	Lutetium-yttrium oxyorthosilicate
MC	Monte Carlo
MCPMT	Multi-channel photomultiplier tube
MRI	Magnetic resonance imaging
NaI(Tl)	Thalium-doped sodium iodide
NEC	Noise equivalent counts
NECR	Noise equivalent count rate
NEMA	National Electrical Manufacturers Association
NM	Nuclear medicine
NPWMF	Non-prewhitening matched filter
PDF	Probability density function
PD	Photodiode
PET	Positron emission tomography
PMT	Photomultiplier tube
PoE	Propagation-of-error
PSPMT	Position-sensitive photomultiplier tube
RSM	Response surface methodology
SCD	Source-to-collimator distance
SF	Scatter fraction
SiPM	Silicon photomultiplier
SKE/BKE	Signal known exactly, background known exactly
SNMMI	Society of Nuclear Medicine and Molecular Imaging
SNR	Signal-to-noise ratio
SPECT	Single photon emission computed tomography
SUV	Standardized uptake value
TBR	Tumor-to-background ratio
TOF	Time-of-flight
UHR	Ultra-High resolution
US	Ultrasound

WB	Whole-body

1. MOTIVATION AND OBJECTIVES

Molecular nuclear medicine (NM) imaging is a very powerful tool for early detection, staging and follow-up of malignancies with an advantage of a high sensitivity compared to other imaging modalities, i.e. X-ray imaging, computed tomography (CT), magnetic resonance imaging (MRI) or ultrasound (US). On the other hand, NM has drawbacks, such as lower intrinsic resolution or lack of anatomical information relative to the techniques mentioned above [1]. Despite of these disadvantages, NM works superior in some cases through its ability of differentiating between healthy tissue and tissue showing pathological abnormalities. All in all, the uptake of the tumor-localizing agent between the tissues indicates functional differences [2]. Thus, the lesion detectability in NM images depends on various factors, such as tumor-to-background ratio (TBR) (related to contrast), count sensitivity (related to noise level) and spatial resolution of the scanner.

The objective of this thesis is to implement Monte Carlo (MC) simulations and response surface methodology (RSM) to the area of molecular nuclear imaging for an ultimate goal of increasing the image and data quality, for a planar camera and a tomographic scanner, respectively. To this end, complex physical processes were simulated based on numerical techniques and efficient experiment designs were employed to assess the effect of chosen parameters on the metrics related to lesion detectability while taking statistical uncertainties throughout the imaging processes into account.

In the first part, our aim was to maximize the lesion detectability of a breast-specific scintimammography camera, assessed by contrast-to-noise ratio (CNR) [3] for a sub-centimeter lesion. CNR is a metric that considers the well-known trade-off between spatial resolution and sensitivity in NM imaging. Hence, CNR was modeled as a function of parameters of a parallel-hole hexagonal lead collimator, i.e. hole length (l), hole diameter (d) and septal thickness (t) and the parameter combination yielding the

highest CNR was seeked by implementing a numerical optimization approach.

Another objective of this study was to understand the behavior of the optimizer for a specific sub-centimeter lesion of fixed size and TBR as its depth in a simplistic geometric phantom representing a compressed breast was changed.

Whereas, the second study concentrates on studying the effect of the activity, the lower energy threshold (LET) and the coincidence time window (CTW) on noise-equivalent-count rate (NECR) of a 3-dimensional (3D) positron emission tomography (PET) camera, since these parameters strongly affect the true, random and scatter event rates and thereby the NECR in 3D PET imaging. NECR demonstrates the effective count sensitivity in PET scanners taking the relative tradeoffs and the contribution of all true, scatter and random coincidences to image noise into consideration [4, 5]. Moreover, it was shown that NECR is dependent on the square of the signal-to-noise ratio (SNR) [6] therefore is an indicator for lesion detectability for PET images.

2. DESIGN AND EVALUATION OF THE COLLIMATOR DIMENSIONS OF A BREAST-SPECIFIC SMALL FIELD-OF-VIEW GAMMA CAMERA USING MONTE CARLO SIMULATIONS AND RESPONSE SURFACE METHODOLOGY

2.1 Introduction

In this work, our aim is to demonstrate a new approach for maximizing the lesion detectability of a scintimammography camera, assessed by CNR, with respect to collimator parameters, i.e. hole length (l), hole diameter (d) and septal thickness (t) using RSM [7] and MC simulations of the physical systems.

A specific camera design was taken as a case study in order to demonstrate the improvements achieved in CNR values for a range of lesions. The method was implemented to optimize the hexagonal collimator of a planar continuous crystal small field-of-view breast scintigraphy camera based on the system developed by Pani *et al.* [8]. This particular system makes use of the high potential of $LaBr_3$:Ce crystal for molecular NM imaging through its high density, low decay time and high light output offering the possibility of improving both the spatial resolution and the energy resolution for low energy imaging [9]. It has a high detector efficiency with a 10 mm thick crystal which is very important for low-count rate type of procedures such as scintimammography. Moreover, the intrinsic resolution of the camera is not the limiting factor for the lesion that is imaged, so that the effect of the collimator choice becomes dominant.

Another objective of this study is to understand the behavior of the optimizer for a specific sub-centimeter lesion of fixed size and TBR as its depth in a simplistic geometric phantom representing a compressed breast is changed.

2.2 Background

This section will provide a summary of data and image quality metrics, breast specific gamma imaging (BSGI), collimators and collimator optimization approaches for BSGI.

2.2.1 Data and Image Quality in Scintillation Camera

2.2.1.1 Spatial resolution. The spatial resolution of a system represents its ability to distinguish between two points after image reconstruction. The measurement is performed by measuring the width of the point spread functions (PSF) of compact radioactive sources by its full-width at half-maximum (FWHM) and full-width at tenth-maximum (FWTM) [10].

2.2.1.2 Sensitivity. Sensitivity is the ability of a gamma camera to use efficiently all of the photons that are available to it in a given time period. It is measured as counts per minute (cpm) per μCi or counts per second (cps) per MBq. The main determinant of intrinsic sensitivity is the crystal thickness. Thicker crystals have greater detection efficiency for higher-energy gamma rays, according to the Eq. 2.1 [11].

$$Sensitivity \propto 1 - e^{-\mu t} \tag{2.1}$$

where t is the crystal thickness and μ is the energy dependent linear attenuation coefficient of the crystal. The intrinsic sensitivity of the camera is therefore a function of gamma ray energy as well as the crystal thickness. Obviously, the width of the energy window and the amount of scatter in the object also affect sensitivity. However, considering the total system sensitivity of the camera, the type of the collimator is the major factor affecting the sensitivity. The higher is the sensitivity, the higher will be the number of the acquired counts, so the less will be the percentage noise in the images.

2.2.1.3 Energy resolution. The detectors should be able to indicate the energy of the incoming annihilation photon such that those that have scattered in the body can be rejected. The ability of the detector to determine the energy of the photon is known as the energy resolution [12]. The energy resolution is conventionally defined as the FWHM divided by the location of the peak of the energy distribution (pulse height spectrum) [10].

2.2.2 Collimators

The collimator is an essential equipment and has a critical role in a gamma camera and SPECT scanner. It influences the number and obliqueness of photons impinging on the crystal, therefore directly affects the system sensitivity and spatial resolution, and consequently the lesion detectability.

Collimators are usually made from lead because of its high atomic number and density. Other materials having higher attenuation coefficients, such as tungsten or depleted uranium, could be more suitable for a collimator, however these are more expensive and/or harder to work with. Since lead is a easy-to-handle material, the collimators should be treated carefully not to be damaged, so that no artifacts in the images are observed.

For different clinical applications, there is the need for different collimator types with different parameter dimensions. The collimator can basically be classified according to the energy levels that are used for or according to their geometrical shapes.

The first group of collimators can be classified as low energy (0-200 keV), medium energy (200-400 keV) and high energy (400-600 keV). The basic difference between these is the septal thickness. Since more energetic photons have a higher penetration ability, thicker septa are needed to stop them.

The latter group of collimators can be further grouped based on their spatial

resolution/count sensitivity trade-off or geometrical shapes:

The geometrical spatial resolution and sensitivity of a collimator depends on the hole geometry and these contribute to the overall performance of the camera. As the hole length gets longer and the hole diameter decreases, a smaller portion of gamma rays impinging on the collimator pass through and reach the crystal. This fact results in a decreased geometrical count sensitivity, but on the other hand in a better collimator resolution. However, a higher sensitivity is more desirable to obtain a lower percentage noise in the image. These facts give rise to the very well-known sensitivity/resolution trade-off in NM. Additionally, another constraint is to keep the hole size smaller than the intrinsic resolution of the camera to prevent the appearance of the hole patterns on the image decreasing its diagnostic value.

In addition to hole size and hole length, a third parameter, the septal thickness, determines the amount of septal penetration, but with a trade-off of sensitivity. Excessive amounts of septal penetration will result in star artifacts, in addition to the degradation in spatial resolution.

Keeping the trade-offs and constraints mentioned above in mind, one of the four collimator types is chosen according the type of acquisition: High sensitivity (HS), general purpose (GP), high resolution (HR) and ultra-high resolution (UHR).

As mentioned above, another classification of collimators can be made according to their geometries:

The great majority of NM studies are performed with parallel-hole collimators (Figure 2.1) which serve for the one-to-one mapping of the emitted rays on the crystal and therefore on the image without magnification, since almost only rays that are perpendicular to the crystal surface can survive through the septa. Without, the use of the collimator, gamma rays from many angles can reach the scintillator deteriorating the spatial mapping ability [11].

Their hole shapes can be round, square or hexagonal. Although round holes are easily manufacturable, dead-spaces between the holes result in decreased count sensitivity. Square holes are also easy to manufacture, however the spatial resolution varies with the direction of the measurement. Therefore, the mostly encountered type is hexagonal hole collimators to maximize sensitivity for a preset spatial resolution value.

To be able to visualize organs that blocked by other organs slant-hole collimators are developed. This kind of collimators have holes that are parallel to each other but not perpendicular to collimator face creating an oblique view. Since these collimators can be brought to close proximity to the patient, they offer an resolution advantage. For example, they are used for cardiac-gated blood-pool scanning and to image the head while eliminating shoulders [11].

A type of collimator specific to small-organ imaging is the pinhole collimator (Figure 2.1). It has cone shape with a very small aperture at the tip. It offers a magnification advantage over other kinds of collimators. The organ should be put as close as possible to the aperture to obtain an increased magnification and better resolution, however this will cause a drop in sensitivity. Another factor affected by this distance is the field-of-view (FoV) size.

Converging collimators operate similar to pinhole ones, in the sense that they also offer magnification of the imaged object with a hole configuration closer together on the object side and farther apart on the crystal side. Whereas, the hole geometry is the opposite for diverging collimators resulting in minimization of large objects being imaged (Figure 2.1).

The last group are fan-beam collimators (Figure 2.2) are designed for a rectangular camera head to image smaller organs like the brain and heart. Their holes are arranged to be parallel to each other along the axis of the patient, however across the patient they are convergent. Therefore, in the transverse axis, the object is magnified as in the case of converging collimators. This hole arrangement facilitates the

maximum use of crystal surface for the data coming from the patient [13].

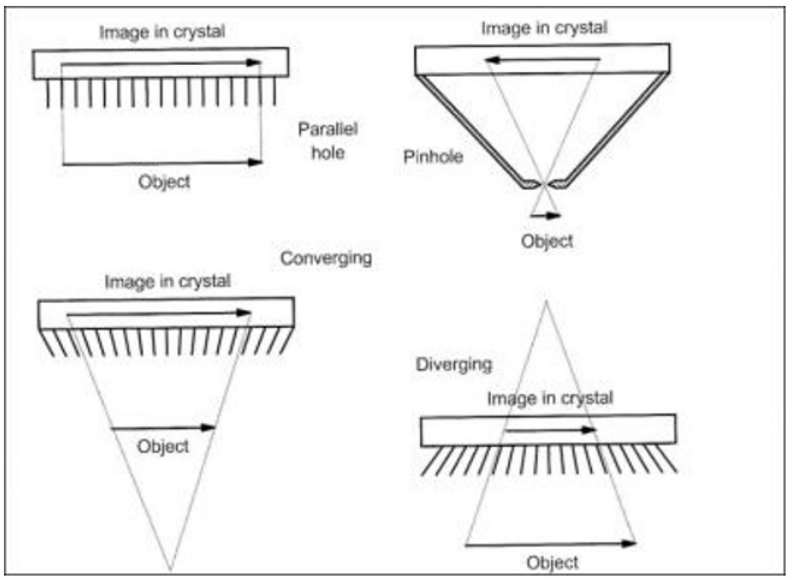


Figure 2.1 Collimator types according to their geometries [14].

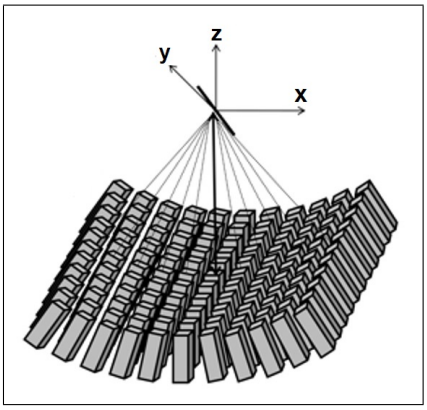


Figure 2.2 Geometry of a fan-beam collimator [15].

2.2.3 Overview: Breast-Specific Gamma-Imaging (BSGI)

X-ray mammography is still the gold standard screening tool for the early detection of breast cancer. However, this modality has significant limitations in terms

of sensitivity and specificity, which even get worse as the with increasing breast density seen in younger patients. Adjunctive modalities to X-ray mammography such as ultrasound, MR imaging, or scintimammography have been proposed to improve the sensitivity of mammography for screening women [16]. A recent meta-analysis performed by Xu *et al.* [17] about the accuracy of scintimammography as an adjunct to diagnostic mammography for detection of breast cancer demonstrated a sensitivity of 83% and specificity of 85%. Rhodes *et al.* [18] found that the addition of BSGI elevates the sensitivity considerably and therefore the cancer detection rate by a factor of 7.5 for dense breasts.

Because of the limitations of X-ray mammography and advantages of BSGI, the detection of breast cancer with single-photon emitting radiotracers using a gamma camera has been a challange of NM imaging [16]. The whole-body systems are suboptimal for breast imaging to be able to detect sub-centimeter lesions, therefore breast-dedicated systems are needed [19].

The tracer used for BSGI is ^{99m}Tc-sestaMIBI, the higher uptake of which in tumors compared to healhty tissue reflects higher vascularity and mitochondrial activity in tumorous tissue [19]. BSGI systems use standard mammographic positioning (craniocaudal and mediolateral oblique) with the breast in direct contact with the gamma camera. They differ mainly by the type (scintillation crystal vs. semiconductor) and configuration (single vs. dual) of the detector [20].

There are high-resolution, small-field-of-view BSGI cameras developed by research groups to allow reliable detection of sub-centimeter tumors [8, 21, 22]. Commercially available BSGI systems include the Dilon 6800 (Dilon Diagnostics), LumaGEM (Gamma Medica), and Discovery NM750b (GE Healthcare).

As a final point, it should be added that the main concern about BSGI is increased radiation doses to the patient (6.5-mSv effective dose equivalent for BSGI vs. 0.7 mSv for X-ray mammography) [23]. This fact creates a need for lower effective doses comparable to that of X-ray mammography. Therefore, studies validating the

diagnostic performance of BSGI at lower doses are ongoing [16].

2.2.4 Overview: Collimator Optimization Studies for Breast Imaging

Collimator design is particularly important for breast-specific gamma imaging which is becoming an important adjunctive procedure for detecting and managing breast cancer and whose clinical impact has been demonstrated in various studies [24–27]. The collimator optimization studies for dedicated breast imaging systems are among those conducted by several groups [28–37] and can be generally classified into two categories as analytical and experimental.

A number of previous studies [30,34,35] adopted the analytical approach where the optimal collimator parameters were derived using approximate functions representing the system response. The analytical approach relies on fixing parameters of the imaging system a priori. For instance, the system resolution is set equal to the lesion size [30, 35] or the collimator resolution [34] is chosen to be equal to the intrinsic resolution of the camera for a preset source-to-collimator distance (SCD). In most cases, the septal penetration is set to 5% *a priori* and the geometric sensitivity of the system is maximized. The analytical technique is a widely used approach, since it is convenient and practical. Nevertheless, setting these parameters *a priori* disregards the fact that the dependence of the overall task performance on the combination of collimator parameters is complex and cannot be easily analytically formulated. In particular, complex realistic modeling becomes very difficult. Another issue with the analytical approach is that formulations may present inaccuracies in cases where the lesion is in close proximity to the collimator surface. Finally, it is very difficult to formulate flexible optimization schemes in which multiple objectives are needed.

As opposed to analytical methods, experimental studies cover physical phantom experiments [29,32] or computer simulations [36,37] to obtain the optimal collimation. These studies are conducted for different collimator types and scanners where the lesion size, depth, TBR and SCD are changed to optimize various image quality metrics. The

possibility to incorporate a high number of parameters to the problem formulation increases the dimension of the search space noticeably. Therefore, one of the major drawbacks of the experimental approach can be regarded as the need for real scans or time consuming complex simulations without a guarantee of obtaining the optimum result. One further disadvantage of the traditional experimentation methods is their inability to detect the interaction between two or more design variables [38]. This creates a need for modeling as well as mathematical schemes essentially for multi-parameter optimization problems.

2.3 Materials and Methods

2.3.1 Design of a Breast-Specific Small Field-of-View Gamma Camera in SIMIND

The breast scintigraphy system was simulated by using SIMIND [39] (Appendix A.1). The simulated camera parameters were chosen to realistically model the actual gamma camera [8]. The continuous $LaBr_3$:Ce crystal of the simulated gamma camera had dimensions of 50.8 mm x 50.8 mm x 10 mm. The intrinsic spatial resolution of the camera was modeled as 1.8 mm and the energy resolution of the system was simulated to be 12% at 140 keV. The collimator material was chosen to be lead with a linear attenuation coefficient μ of 26.32 cm^{-1} at 140 keV energy for ^{99m}Tc.

This particular system makes use of the high potential of lanthanum bromide ($LaBr_3$:Ce) crystal for low energy nuclear medicine (80-300 keV). This crystal offers the possibility of improving both the spatial resolution and the energy resolution for low energy imaging through its high density, low decay time and high light output [9]. A comparison with other crystals used in single photon gamma imaging is provided below in Table 2.1.

The simulated system was validated in terms of spatial resolution and sensitivity using a GP hexagonal collimator (*hole diameter*: 1.5 mm, *septal thickness*: 0.2 mm,

hole length: 22 mm) and a HR collimator (*hole diameter*: 1.5 mm, *septal thickness*: 0.2 mm, *hole length*: 40 mm) for ±10% energy window. The spatial resolution was tested with a point source that was placed at varying SCD (0 cm, 5 cm and 10 cm from the collimator surface). The spatial resolution values were computed as the FWHM of the Gaussian curve fitted to the point spread function of the point source. Whereas, the detector sensitivity was measured by placing a 1000 μCi ^{99m}Tc source close to the collimator surface in the center of the field-of-view. For validation, the simulated spatial resolution and sensitivity values were compared with the experimental data taken from [8].

Table 2.1
Comparison of $LaBr_3$:Ce crystal with other crystals used as scintillators in single photon gamma imaging [40].

Scintillator	**Density (g/cm^3)**	**Effective Atomic Number Z_{eff}**	**Wavelength of Maximum Emission (nm)**	**Principal Decay Constant (μs)**	**Relative Light Output (% of NaI(Tl))**
NaI(Tl)	3.67	51	415	0.230	100
CsI(Na)	4.51	54	420	0.630	85
CsI(Tl)	4.51	54	540	0.680	45 (118*)
$LaBr_3$(Ce)	*5.30*	*47*	*360*	*0.025*	*160*

* Total light output. The effective signal for CsI(Tl) is only 45% of NaI(Tl).

2.3.2 Breast Scintigraphy Simulations

In this study, the energy window was set to accept energy levels between 126 keV and 154 keV and the collimator hole shape was chosen to be hexagonal.

The breast was modeled as a cylinder in a craniocaudal position and assumed to be compressed to a thickness of 6 cm [35] and has a diameter of 10 cm. The breast phantom was simulated to be filled with aqueous ^{99m}Tc with an absolute activity concentration of 100 nCi/cc. This activity level was chosen based on the results of Mann *et al.* [41], where the quantification of radiotracer uptake in the breast tissue was

obtained by analyzing images acquired using a dedicated breast SPECT-CT scanner following injection of 25 mCi ^{99m}Tc-sestamibi in accordance with SNMMI [42] and EANM [43] breast scintigraphy protocols. The lesion was modeled as a sphere of 5 mm diameter located on the longitudinal axis of the cylindrical breast phantom at depths of 3 cm or 5 cm according to the two optimization problem formulations. These depth values also correspond to the distance of the lesions from the collimator surface since the detector head can be brought to close proximity to touch the breast (Figure 2.3). The activity uptake ratio of the lesion and normal tissue was reported to be between 3:1 and 12:1 [44], with a mean value of 6:1 [44–46]. Based on this information, a ^{99m}Tc concentration ratio of 6:1 was used for the lesion and the breast tissue, such that the lesion was assumed to have an activity concentration of 600 nCi/cc.

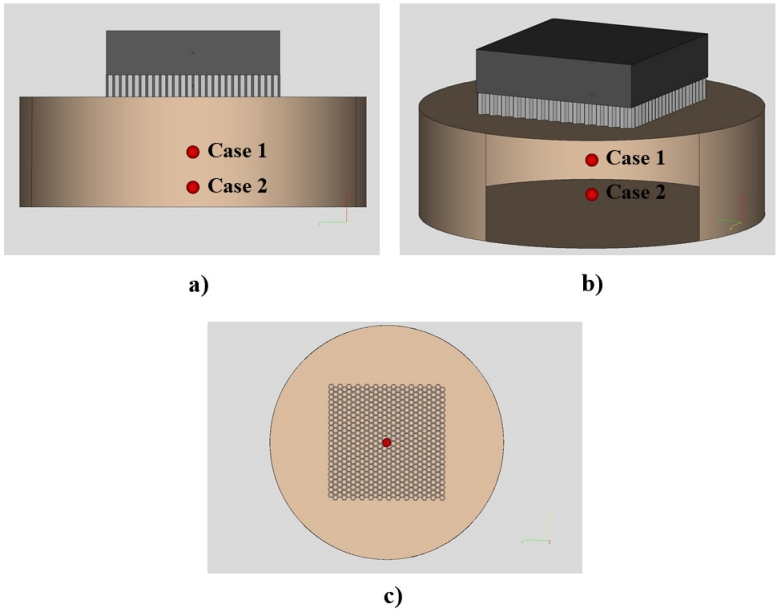


Figure 2.3 **a)** Side view, **b)** Oblique view and **c)** Bottom view of the camera and the breast phantom for a craniocaudal projection of the breast. Red dots in a) and b) represent the lesions and their locations. Case 1 and Case 2 stands for 3 cm depth optimization case and 5 cm depth optimization case, respectively.

For the experiments, the image matrix size was computed and set according to the intrinsic resolution of the camera. The matrix size was chosen as 64x64 to avoid aliasing such that any lesion as small as the intrinsic resolution of the camera (1.8 mm) occupies at least 2 pixels.

For each run, two simulations were performed; one for the breast phantom and one for the lesion phantom. The simulations were run with a high number of photon histories (10^8), in order to be able to obtain low noise data with good statistical uncertainty [47]. Therefore, after the two images were superimposed, Poisson noise was added to the image data using MATLAB corresponding to the count level obtained for the simulated activity, which was also scaled according to a fixed acquisition time of 10 minutes. The count density values in the images were obtained by analyzing the regions of interest representing breast tissue without pathology and expressed as counts/cm^2 per total imaging time per total injected activity [32].

2.3.3 Calculation of the System Response

The detection limit of an imaging system depends on the lesion to background contrast and the noise in the background. CNR is a metric that takes into consideration both the resolution and the sensitivity, the well-known trade-off in NM imaging. Moreover, CNR was shown to be correlated with the non-prewhitening matched filter (NPWMF) numerical observer detectability index [48] to predict detection performance of human observers in signal known exactly, background known exactly (SKE/BKE) situations where the only variation in signal and background comes from noise [49, 50]. CNR was calculated according to the Rose model [3] using the mean pixel intensity (rather than the maximum intensity) over the same spatial region matching the lesion size for all collimators (Eq. 2.2). The calculations were performed by using MATLAB.

$$CNR_l = \frac{|C_l|}{C_{noise}} \approx |C_l| \times d_l \times \sqrt{R_0 \times t} \tag{2.2}$$

where C_l and C_{noise} are lesion and noise contrast, respectively. d_l is the diameter of the lesion, R_0 is the uniform background counting rate measured in counts per second per cm^2 and t is the imaging time.

2.3.4 Implementation of RSM on Breast Scintigraphy Collimator Design Optimization

The workflow of RSM is sequential [7, 38, 51] (Appendix B.1). Along the RSM implementation, we used the Design-Expert software [52] for design of experiments (DoE), the response model fit and optimization steps. At the first stage, screening experiments were conducted to analyze the design space and to investigate the effect of each individual factor (Table 2.2) on the system response over a large range and also over shorter intervals in the given range. As a result, a first guess for parameter levels was found (values in Table 2.3 denoted as initial). Next, our objective was shift the design space towards the general vicinity of the optimum starting from an initial guess of parameter combination by using a first degree model Eq. B.2, where n was taken as 3 and the low, mean and high level of each parameter were evenly spaced and coded as -1, 0 and 1, respectively.

Table 2.2
Range for the screening experiments.

	Low Level	**High Level**
X_1 - Hole diameter (cm)	0.100	0.200
X_2 - Septal thickness (cm)	0.015	0.035
X_3 - Hole length (cm)	1.00	4.00

Table 2.3
Initial guess of parameters and values near the optima observed at the final iteration of the gradient ascent.

	Lesion @ 3 cm		**Lesion @ 5 cm**	
	Initial	**Final**	**Initial**	**Final**
X_1 - Hole diameter (cm)	0.125	0.125	0.112	0.105
X_2 - Septal thickness (cm)	0.025	0.028	0.025	0.022
X_3 - Hole length (cm)	1.000	1.151	1.375	1.464

At his phase, a two-level full factorial (2^3) experiment with 5 center runs [51] was conducted to build a first-order model (Table 2.4). The center runs contribute

to reduce the prediction variance over the design space. To approach the optimum, the gradient ascent algorithm was implemented. The new variable combination on the path of gradient ascent was computed by translating the current values by the step size Δx_i^* calculated as in Eq. 2.3 in each direction and CNR was computed along the path until no further increase in CNR was observed. When the last point of the gradient ascent direction was reached (values in Table 2.3 denoted as final), another first-order equation was fitted to the data to check for the curvature. In case of lack-of-fit due to presence of curvature, a second-order model was designed around the vicinity of the maximum response.

Table 2.4
Two-level factorial design of experiments with center runs.

Exp. #	**Coded Variables**		
	x_1	x_2	x_3
1	-1	-1	-1
2	-1	-1	1
3	-1	1	1
4	1	-1	-1
5	1	-1	1
6	1	1	-1
7	-1	1	-1
8	1	1	1
9	0	0	0
10	0	0	0
11	0	0	0
12	0	0	0
13	0	0	0

-1: Low level, 0: Mean level, 1: High Level

$$\Delta x_i^* = \rho \frac{\beta_i}{\| \beta \|} = \rho \frac{\beta_i}{\sqrt{\sum_{j=1}^{3} \beta_j^2}} \tag{2.3}$$

where ρ is a coefficient such that any positive multiple of it will lead to points on the gradient ascent direction.

At the last stage, the second-order experiments were designed by the Box-Behnken method [32] using the ranges of parameters given in Table 2.6 around the vicinity of the maximum response. Box-Behnken design (BBD) is nearly rotatable and requires 3 levels of each parameter (Table 2.5). Its geometry suggests a sphere, the center of which coincides with the center of the design space. The peripheral design points lie where the sphere first touches the wireframe as you let it grow and they lie at an equal distance to the center point (Figure B.1c). BBD was chosen in particular to avoid factor combinations that are extreme, such that the corner points of the cube in Figure B.1c. Moreover, it offers a considerable efficiency advantage by requiring only 17 runs for 3 factors [53] (5 of them being center runs again to serve the purpose of increasing predictive reliability) compared to the three-level full (3^k) factorial design that would suggest 27 for 3 factors (k=3). The actual levels of each control variable for BBD were given in Table IV. The obtained CNR values were fitted to the general second-order polynomial (Eq. B.3) to model the curvature and regression coefficients were obtained, where the number of the independent variables (n) was again taken to be 3.

Significance of the regression model, individual model coefficients and interaction between them were statistically analyzed performing analysis of variance (ANOVA). The distribution of the residuals between the observed and predicted CNR values (ε) was analyzed for the quadratic model to check for necessity for normalization of the data before starting the optimization process.

Table 2.5
Box-Behnken design of experiments with center runs.

Exp. #	Coded Variables		
	x_1	x_2	x_3
1	-1	-1	0
2	1	-1	0
3	-1	1	0
4	1	1	0
5	-1	0	-1
6	1	0	-1
7	-1	0	1
8	1	0	1
9	0	-1	-1
10	0	1	-1
11	0	-1	1
12	0	1	1
13	0	0	0
14	0	0	0
15	0	0	0
16	0	0	0
17	0	0	0

-1: Low level, 0: Mean level, 1: High Level

For the optimization step (Appendix B.2.2), the response was converted into a desirability function d [54] over the interval [0,1]. *d=0* and *d=1* represent the completely undesirable response and the fully desirable response, respectively. The desirability function was defined as in Eq. B.12 to maximize the response, where the value of ω was taken as 1 in this study to model the desirability as a ramp function. The greatest desirability was then used by the optimizer to find the combination of optimal parameters maximizing the CNR. In our study, the simplex in R^3 was a tetrahedron.

Table 2.6
Levels of parameters for the Box-Behnken design.

	Optimization Formulation (Lesion Depth)					
	3 cm			**5 cm**		
	-1	**0**	**1**	**-1**	**0**	**1**
X_1 - Hole diameter (cm)	0.120	0.125	0.130	0.090	0.100	0.110
X_2 - Septal thickness (cm)	0.025	0.030	0.035	0.015	0.020	0.025
X_3 - Hole length (cm)	1.00	1.15	1.30	1.20	1.40	1.60

-1: Low level, 0: Mean level, 1: High Level

This whole procedure was repeated to obtain the optimal collimators at both lesion depths.

2.3.5 Performance Assessment of Collimators

Three performance measures of the collimator affecting the image quality can be counted as the sensitivity, the spatial resolution and the septal penetration. In this study, the collimator hole configuration was chosen to be hexagonal (Figure 2.4).

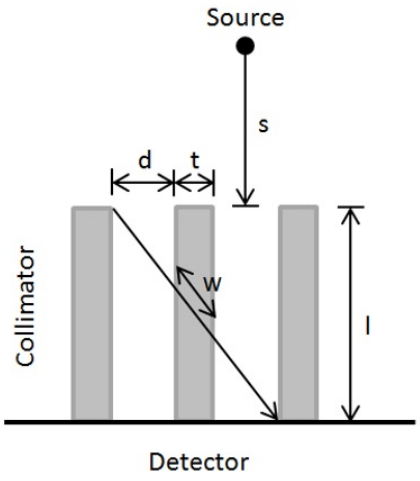


Figure 2.4 Cross-section of a parallel-hole collimator.

For this kind of collimators, the geometric efficiency of the collimator g_c is defined as Eq. 2.4 [55].

$$g_c = \left(\frac{A_{open}}{4\pi l_e^2}\right)\left(\frac{A_{open}}{A_{unit}}\right) \tag{2.4}$$

where the effective hole length, l_e, is a function of the hole length (l) and the linear attenuation coefficient μ of the collimator material and can be expressed as $l_e = l - 2\mu^{-1}$. Putting Eq. 2.5 and Eq. 2.6 for A_{open} and A_{unit}, respectively;

$$A_{open} = \frac{\sqrt{3}}{2}d^2 \tag{2.5}$$

$$A_{unit} = \frac{\sqrt{3}}{2}(d+t)^2 \tag{2.6}$$

the geometric efficiency of the collimator can be rewritten as

$$g_c = \left(\frac{\sqrt{3}}{8\pi l_e^2}\right)\left(\frac{d^4}{(d+t)^2}\right) \tag{2.7}$$

.

where d is the hole diameter and t is the septal thickness of the collimator as shown in Figure 2.4. Further, the geometric efficiency of the collimator is converted to sensitivity in units of cpm/μCi [56].

$$S = \eta g_c \left(2.2 \times 10^6\right) \tag{2.8}$$

where η is the number of gamma rays emitted per nuclear decay.

The resolution of the collimator (R_c) depends on its hole diameter (d), effective hole length (l_e) and source to collimator distance (s) and is analytically determined as follows [55].

$$R_c = \frac{d\,(l_e + s)}{l_e} \tag{2.9}$$

The total system resolution (R_s) is then calculated by combining the intrinsic resolution of the detector (R_i) and the collimator resolution (R_c) as follows

$$R_s = \left(R_i^2 + R_c^2\right)^{1/2} \tag{2.10}$$

Lastly, the percentage septal penetration (SP) of a collimator is calculated as in Eq. 2.11, where w is defined as the minimum path length [55] and can be approximated to Eq. 2.12.

$$SP = 100 * \ exp\,(-\mu w) \tag{2.11}$$

$$w = \frac{t\sqrt{(2d + t)^2 + l^2}}{2d + t} \tag{2.12}$$

2.4 Results

2.4.1 Validation of the Gamma Camera System

The overall detector sensitivity for a ±10% energy window was found as 494 cpm/μCi and 138 cpm/μCi for the GP and HR collimators with estimated errors of

less than 1% as the result of validation simulations. The spatial resolution values (Figure 2.5) were found to show a good agreement with those given in [8] based on real measurements of the $LaBr_3$:Ce camera with a maximum estimated error of 7% within the relevant interval of 0 - 5 cm for SCD.

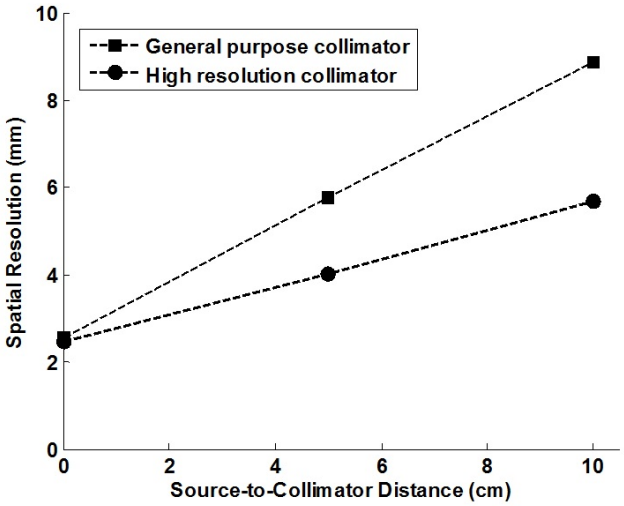


Figure 2.5 Spatial resolution vs. source-to-collimator distance for the camera.

2.4.2 Second-Order Response Surface Model

The CNR values obtained from the experiments (Box-Behnken design) are presented in Table 2.7 and the second-order model coefficients are summarized in Table 2.8.

ANOVA results revealed that the models were sufficient (p-values of 0.001 and 0.002) to represent the relationship between the collimator parameters and CNR for both lesion depths of 3 cm and 5 cm, respectively (Table 2.9 and Table 2.10). The analysis of residuals yielded no need for normalization of the data for both models.

For the range of values given Table 2.6, the *hole length* was found to be most significant effect of the model for the lesion at a depth of 3 cm with a p-value of 0.028, while the *septal thickness* presented the largest effect on CNR for the second model.

Table 2.7
Experimental design for the Box-Behnken design in terms of actual factors and the corresponding CNR yield.

	Optimization Formulation (Lesion Depth)							
	3 cm				**5 cm**			
Exp. #	X_1	X_2	X_3	**CNR**	X_1	X_2	X_3	**CNR**
1	0.120	0.025	1.15	**3.3164**	0.090	0.015	1.40	**1.6234**
2	0.130	0.025	1.15	**3.2926**	0.110	0.015	1.40	**1.5223**
3	0.120	0.035	1.15	**3.2641**	0.090	0.025	1.40	**1.6200**
4	0.130	0.035	1.15	**3.2797**	0.110	0.025	1.40	**1.6434**
5	0.120	0.030	1.00	**3.3055**	0.090	0.020	1.20	**1.6411**
6	0.130	0.030	1.00	**3.2869**	0.110	0.020	1.20	**1.5908**
7	0.120	0.030	1.30	**3.2349**	0.090	0.020	1.60	**1.5840**
8	0.130	0.030	1.30	**3.2835**	0.110	0.020	1.60	**1.6760**
9	0.125	0.025	1.00	**3.2397**	0.100	0.015	1.20	**1.4713**
10	0.125	0.035	1.00	**3.3093**	0.100	0.025	1.20	**1.6489**
11	0.125	0.025	1.30	**3.3093**	0.100	0.015	1.60	**1.6224**
12	0.125	0.035	1.30	**3.2085**	0.100	0.025	1.60	**1.5996**
13	0.125	0.030	1.15	**3.3480**	0.100	0.020	1.40	**1.6692**
14	0.125	0.030	1.15	**3.3232**	0.100	0.020	1.40	**1.6757**
15	0.125	0.030	1.15	**3.3225**	0.100	0.020	1.40	**1.6899**
16	0.125	0.030	1.15	**3.3381**	0.110	0.020	1.40	**1.6546**
17	0.125	0.030	1.15	**3.3150**	0.110	0.020	1.40	**1.6740**

X_1: Hole diameter (cm), X_2: Septal thickness (cm), X_3: Hole length (cm)

For both models, the *hole diameter* presented the weakest effect on CNR, with p-values of 0.59 and 0.58.

The two factor interactions, incorporating a form of curvature to the models, are shown in Figure 2.6. For the 3 cm lesion depth model, the terms X_1X_3 (Figure 2.6b) and X_2X_3 (Figure 2.6c) were found to be significant interaction terms with p-values of 0.041 and $<$0.001, respectively, whereas for the 5 cm lesion depth case, all interaction terms (X_1X_2 (Figure 2.6d), X_1X_3 (Figure 2.6e) and X_2X_3 (Figure 2.6f) were found to have a significant effect on CNR having p-values of 0.024, 0.013 and

Table 2.8
Coefficients for the second-order models in terms of coded factors.

	Optimization Formulation (Lesion Depth)	
	3 cm	**5 cm**
	Model Coefficient	**Model Coefficient**
β_0	3.300	1.679
β_1	2.715e-03	-4.500e-03
β_2	-0.012	0.034
β_3	-0.013	0.016
β_{12}	9.843e-03	0.031
β_{13}	0.017	0.036
β_{23}	-0.043	-0.050
β_{11}	-0.015	-0.016
β_{22}	-0.026	-0.054
β_{33}	-0.037	-0.033

x_1: Hole diameter (cm), x_2: Septal thickness (cm),
x_3: Hole length (cm)

0.002, respectively (Table 2.9 and Table 2.10). For both models, *septal thickness* and *hole length* showed the heaviest interaction. In Figure 2.6, the interaction between factors is demonstrated by their intersection, since it indicates a change in a factor's effect on the systems response depending on the level of the other factor. The relative impact of the interaction effects X_1X_3 and X_2X_3 for both collimators were found to surpass the significance of the corresponding main effects since their model coefficients are larger (Table 2.8), leaving limited importance to the main effects solely. As a consequence, the optimal collimator parameter values were found to heavily depend on these interactions.

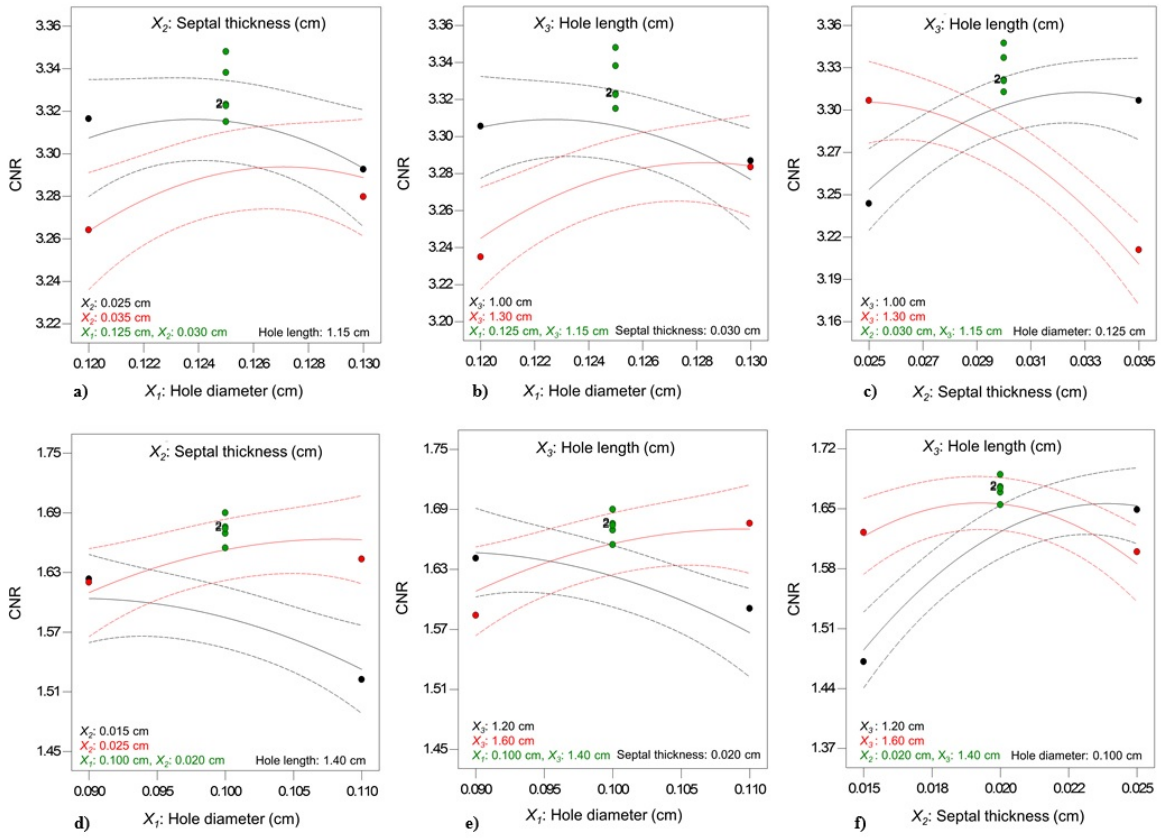


Figure 2.6 Two factor interaction plots of collimator parameters. **a)**, **d)** Hole diameter and septal thickness, **b)**, **e)** hole diameter and hole length, and **c)**, **f)** septal thickness and hole length, for 3 cm and 5 cm lesion depth optimization case, respectively. The black, red and green dots represent the design points. The black (red) solid line is observed by changing the parameter on the x-axis while keeping the other at its lower (higher) level, where the third parameter is kept at its 0-level for each plot (**a)** hole length=1.150 cm, **b)** septal thickness=0.030 cm, **c)** hole diameter=0.125 cm, **d)** hole length=1.200 cm, **e)** septal thickness=0.020 cm, **f)** hole diameter=0.100 cm). The black and red dashed lines represent confidence interval bands of the CNR response. Since the black and red data points lie within the confidence bands, it can be said that there is no significant difference between the response observed from the simulations and the model response. The green dots indicate the data points at which both interaction parameters are at their 0-levels. An interaction occurs when the response differs depending on the setting of the other and is indicated by non-parallel/intersecting curves. Therefore, the strongest interaction among the parameter pairs can be said to be present in **c)** and **f)** between septal thickness and hole length within the relevant intervals.

The quadratic main effects of hole length and septal thickness, coded as X_2^2 and X_3^2, were significant for both models with p-values of 0.005 and <0.001 and, 0.001 and 0.016, for the models created for 3 cm and 5 cm deep lesions, respectively. X_1^2 having a p-value of 0.055 was found to have a moderate significant effect on CNR for the 3 cm model. Significant quadratic main effects with negative coefficients (Table 2.8) indicate a decrease in CNR when their values deviate from their 0 levels.

Table 2.9
ANOVA results for the quadratic response surface CNR model of the optimization case for lesion at 3 cm SCD.

Source	Sum of Squares	df	Mean Square	F Value	p-value Prob>F	
Model	0.022	9	2.421e-03	13.38	0.001	significant
X_1 - *Hole diameter*	5.898e-05	1	5.898e-05	0.33	0.59	
X_2 - *Septal thickness*	1.161e-03	1	1.161e-03	6.42	0.039	
X_3 - *Hole length*	1.384e-03	1	1.384e-03	7.65	0.028	
X_1X_2	3.875e-04	1	3.875e-04	2.14	0.19	
X_1X_3	1.129e-03	1	1.129e-03	6.24	0.041	
X_2X_3	7.258e-03	1	7.258e-03	40.12	<0.001	
X_1^2	9.541e-04	1	9.541e-04	5.27	0.055	
X_2^2	2.865e-03	1	2.865e-03	15.84	0.005	
X_3^2	5.642e-03	1	5.642e-03	31.19	<0.001	
Residual	1.266e-03	7	1.809e-04			
Lack of Fit	*5.532e-04*	*3*	*1.844e-04*	*1.03*	*0.47*	*not significant*
Pure Error	*7.129e-04*	*4*	*1.782e-04*			
Cor Total	0.023	16				

2.4.3 Optimal Collimator Parameters

The results show that, for a lesion depth of 3 cm, the combination of hole length of 1.137 cm, septal thickness of 0.029 cm and hole diameter of 0.125 cm are the optimal solutions that provide the highest CNR values. Whereas, the optimal parameters were found to be 1.440 cm, 0.022 cm and 0.104 cm in the same order for 5 cm deep lesion.

The response surface iso-desirability contour plots of the 3 cm deep lesion model are given Figure 2.7. The smallest iso-desirability contour is where the maximum predicted CNR is located. A more elliptical rather than a circular shape of the contours in Figure 2.7 is another indicator for a stronger interaction between parameters. The predicted maximum CNR values were later validated by performing simulations at the

Table 2.10
ANOVA results for the quadratic response surface CNR model of the optimization case for lesion at 5 cm SCD.

Source	Sum of Squares	df	Mean Square	F Value	p-value Prob>F	
Model	0.050	9	5.576e-03	11.90	0.002	significant
X_1 - *Hole diameter*	1.620e-04	1	1.620e-04	0.35	0.58	
X_2 - *Septal thickness*	9.282e-03	1	9.282e-03	19.81	0.003	
X_3 - *Hole length*	2.109e-03	1	2.109e-03	4.50	0.072	
X_1X_2	3.875e-03	1	3.875e-03	8.27	0.024	
X_1X_3	5.062e-03	1	5.062e-03	10.81	0.013	
X_2X_3	0.010	1	0.010	21.43	0.002	
X_1^2	1.145e-03	1	1.145e-03	2.44	0.16	
X_2^2	0.012	1	0.012	26.12	0.001	
X_3^2	4.645e-03	1	4.645e-03	9.92	0.016	
Residual	3.279e-03	7	4.685e-04			
Lack of Fit	*2.633e-03*	*3*	*8.777e-04*	*5.43*	*0.068*	*not significant*
Pure Error	*6.464e-04*	*4*	*1.616e-04*			
Cor Total	0.053	16				

optimal parameter levels.

The theoretical values for collimator sensitivity, spatial resolution and septal penetration for the reference and optimal collimators are summarized in Table 2.11 for comparison. The percentage septal penetration for the optimal collimators was calculated for 3 cm and 5 cm lesion depths as 4.06% and 2.54%, respectively. The system spatial resolution for the collimators optimized at 3 cm and 5 cm depths was found to be 5.11 mm and 5.17 mm, respectively. As a result of simulations, the sensitivity values for the two collimators for an energy window width of 20% were found as 1286 cpm/μCi and 539 cpm/μCi. These values yielded an absolute error of 3.03% and 0.19% with respect to the analytically calculated theoretical values of 1248 cpm/μCi and 540 cpm/μCi. The collimator for 3 cm lesion depth provided a 2.35-fold and 8.05-fold in-

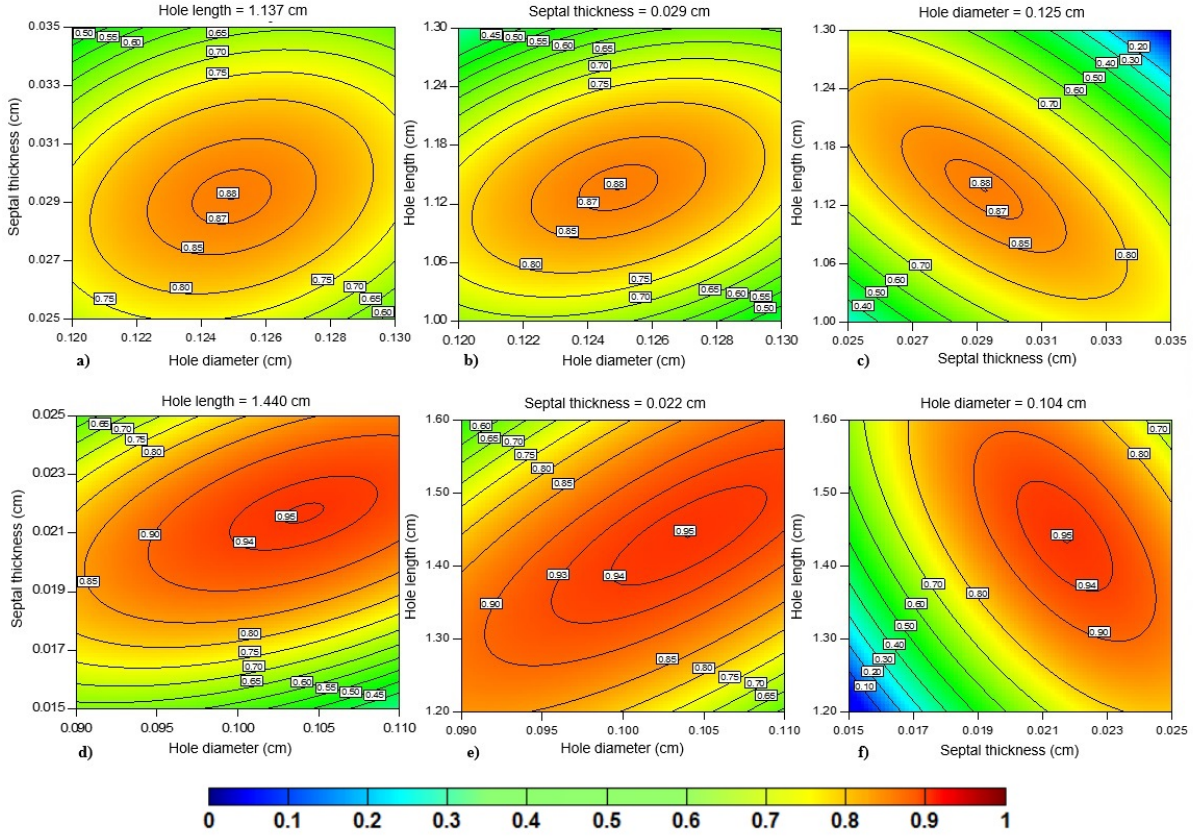


Figure 2.7 Iso-desirability contours. **a)**, **d)** Hole diameter vs. septal thickness, **b)**, **e)** hole diameter vs. hole length, and **c)**, **f)** septal thickness vs. hole length, for CNR models developed for lesions lying at a depth of 3 cm and 5 cm, respectively. The third parameter was kept at its optimal level for each plot (**a)** hole length=1.137 cm, **b)** septal thickness=0.029 cm, **c)** hole diameter=0.125 cm), **d)** hole length=1.440 cm, **e)** septal thickness=0.022 cm, **f)** hole diameter=0.104 cm).

crease in sensitivity with respect to the GP and HR collimators, respectively, whereas the gain was found to be 1.02 and 3.48 for the collimator designed for 5 cm lesion depth.

Table 2.12 also summarizes the count densities in the images acquired with hexagonally modeled breast-specific and optimized collimators together with the resultant CNRs for both lesion depths. The relative increase in CNR was quantified to be in the range of 6-73% and 4-34% with respect to the reference collimators for the lesions with TBR of 6:1 at a depth of 3 cm and 5 cm, respectively.

Table 2.11
Sensitivity, septal penetration and spatial resolution for optimum and other breast specific collimators at both 3 cm and 5 cm depths.

Collimator	Hole Size (cm)	Septal Thickness (cm)	Hole Length (cm)	Collimator Sensitivity (cpm/μCi)	Septal Penetration (%)	Collimator Resolution (mm)	
						@ 3 cm	@ 5 cm
A	0.112	0.048	0.940	1124	1.06	5.01	7.60
B	0.219	0.031	2.130	1190	2.25	5.39	7.52
C	0.254	0.030	2.500	1198	2.34	5.68	7.78
D	0.100	0.020	1.800	319	1.30	2.74	3.90
GP	0.150	0.020	2.200	530	2.58	3.62	5.03
HR	0.150	0.020	4.000	155	0.14	2.65	3.41
OPT. (3 cm)*	**0.125**	**0.029**	**1.137**	**1248**	**4.06**	**4.78**	**7.14**
OPT. (5 cm)**	**0.104**	**0.022**	**1.440**	**540**	**2.54**	**3.33**	**4.85**

* Collimator optimized for a lesion at 3 cm depth.
** Collimator optimized for a lesion at 5 cm depth.

Table 2.12
Performance comparison of optimum and other breast specific collimators at both 3 cm and 5 cm depths.

Collimator	Hole Size (cm)	Septal Thickness (cm)	Hole Length (cm)	Count Density*** (counts/cm^2)	CNR	
					@ 3 cm	@ 5 cm
A	0.112	0.048	0.940	4124	3.14	1.40
B	0.219	0.031	2.130	4374	2.93	1.44
C	0.254	0.030	2.500	4386	2.76	1.35
D	0.100	0.020	1.800	1183	2.70	1.61
GP	0.150	0.020	2.200	1992	2.89	1.61
HR	0.150	0.020	4.000	579	1.93	1.25
OPT. (3 cm)*	**0.125**	**0.029**	**1.137**	**4710**	**3.34**	**1.52**
OPT. (5 cm)**	**0.104**	**0.022**	**1.440**	**2117**	**3.03**	**1.68**

* Collimator optimized for a lesion at 3 cm depth.
** Collimator optimized for a lesion at 5 cm depth.
*** The total counts in the images can be obtained by multiplying the observed count densities by the imaging area of the detector (5 cm x 5 cm).

For further interpretation of our findings, test the performance of the optimal collimator (optimized for 3 cm SCD) for various lesion types, and compare it with other breast collimators, we simulated lesions of diameters from 0.4 to 1 cm and TBR values between 3:1 and 13:1 at 3 cm depth (Figure 2.8). From these simulations, iso-CNR curves, representing equal CNR levels, were obtained by fitting the CNR values to second-order polynomials. For this analysis, the activity concentration in the breast tissue was kept again at 100 nCi/cc where the activity in the lesion was changed according to lesion size and TBR. In all subplots of Figure 2.8, the area shaded from yellow to green corresponding to CNR levels between 3 and 5 represent the critical region for detectability [50]. The contrast-detail curves in Figure 2.8 present the shift of the critical region for detectability towards the smaller lesion diameter and lower TBR direction when the optimal collimator is used. This fact indicates a larger area within the visible region over the range of various lesion types.

Additionally, Figure 2.9 demonstrates the collimators' performances at various lesion depths ranging from 1 cm to 5 cm for TBR values from 3:1 to 12:1. This figure clearly demonstrates that the collimator optimized for 3 cm SCD outperforms the one optimized for 5 cm SCD for a lesion lying at 3 cm depth for all TBR values. Likewise, the collimator optimized for 5 cm SCD has a better performance than the one optimized for 3 cm SCD for a lesion lying 5 cm deep.

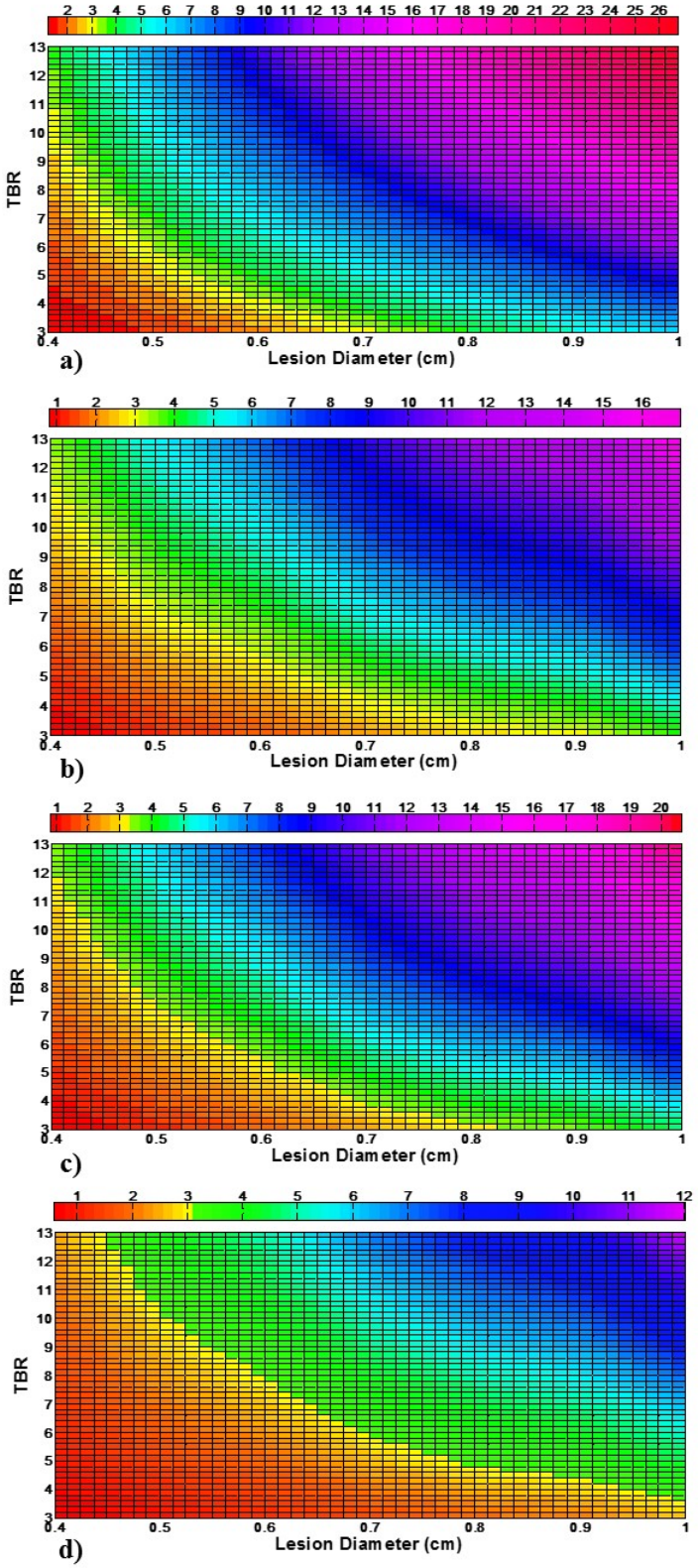


Figure 2.8 Iso-CNR plots with respect to TBR and lesion diameter for a lesion depth of 3 cm obtained with **a)** the optimum (optimized for 3 cm SCD) collimator, **b)** collimator D, **c)** collimator GP and **d)** collimator HR.

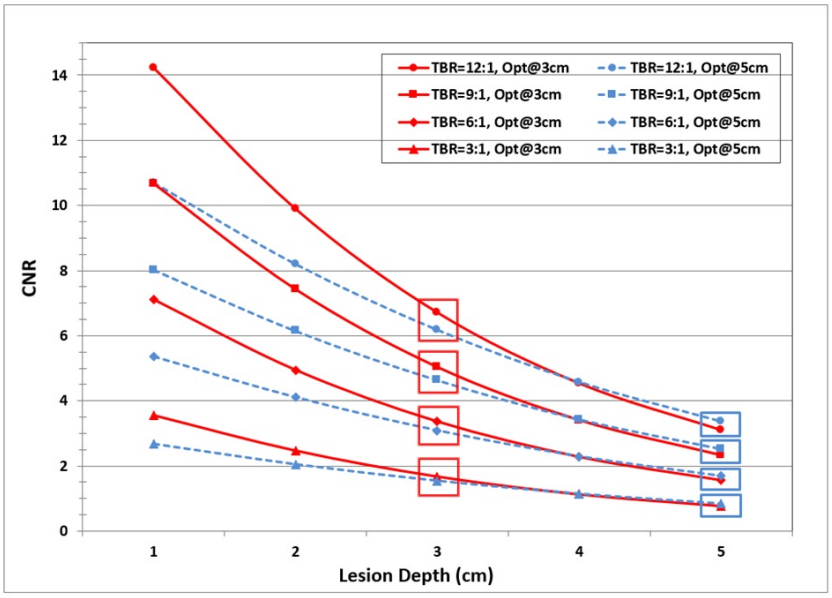


Figure 2.9 Collimators'performances at various lesion depths ranging from 1 cm to 5 cm for TBR values from 3:1 to 12:1.

2.5 Discussion and Conclusion

In this study, we used RSM to select the optimal collimator parameters for a scintimammography system to detect sub-centimeter lesions using MC simulations. For this purpose, the breast was modeled as a cylinder with a diameter of 10 cm and a thickness of 6 cm. The lesion was assumed to be a sphere with a 5 mm diameter. The activity concentration ratio of the lesion to the breast was taken as 6:1. The absolute activity concentration for the breast and the lesion was kept at realistic values and were taken as 100 nCi/cc and 600 nCi/cc, respectively. For this task, CNR was chosen as a figure-of-merit for lesion detectability, since the changes in lesion size, contrast and image noise were shown to have equivalent effects on the observers' detectability performance [57].

As a result, the quadratic models were found to be sufficient to represent the relationship between the collimator parameters and CNR since ANOVA yielded no significant lack-of-fit for the second-order models of the fitted data for both lesion depths.

The combination of optimal collimator parameters were calculated to offer percentage septal penetration values below the tolerance value of 5% [58]. It was shown that, the optimized collimators provide a substantial increase in count sensitivity which can be directly related to reduction in administered dose or data acquisition time to achieve the same detectability since these are related to sensitivity reciprocally.

We observed that the optimization resulted in system resolutions very close to the lesion sizes at corresponding depths. Based on this fact, the optimized collimator parameters can be regarded to be sensitive to lesion depth to compensate the well-known fact of degradation in resolution with increasing SCD. Additionally, it can be concluded that the optimal collimator parameters do not depend on TBR, which only affects the absolute level of CNR.

The performance of the optimized collimators for both cases was found to be superior compared to the others used for breast imaging (Table 2.12). However, no visual benefit of using the optimized collimator could be demonstrated for the current low uptake value of 6:1, since the highest CNR value yielded by the optimized collimator was under the safe upper visibility threshold of 5. It should be noted that this finding is supported by the study of Cinti *et al.* [59] where the breast thickness of 6 cm was stated to be critical because of the elevated background it causes. This fact yielded unsatisfactory results for the cameras investigated by the researchers at clinical TBR values for 5 mm sized lesions (signal-to-noise ratio$<$5). Additionally, Buvat *et al.* [29] specified larger lesions as borderline in terms of detectability for the different collimators they studied.

Our findings presented in Figure 2.8a exhibit that a 5 mm lesion with a TBR value of 9:1 is detectable with the optimized collimator, since the CNR value reaches 5. However, other collimators need higher TBR values so that the lesion would be detectable, for HR collimator it will not be possible to detect the lesion even with the highest clinically relevant TBR value of 12:1. Besides, the smallest lesion having a TBR value of 6:1 imaged with the optimal collimator at 3 cm SCD, for which CNR reaches the value 5 was found to be of size 6.1 mm.

As given in Table 2.12, CNR values observed for 5 mm lesions lying 5 cm deep were even below the lower threshold of 3, even using the optimized collimator. After all, to detect those that lie deeper than the half of the breast thickness (3 cm), the data can be collected sequentially from the opposite sides of the breast or with opposite detectors using the optimized collimator for 3 cm depth. Therefore, we make the practical assumption that the optimization performed for a 3 cm deep lesion can be considered as the worst-case. However, improving tumor uptake with the development of target-specific radiopharmaceuticals with higher tumor affinity as an alternative to ^{99m}Tc-sestamibi should facilitate the detection of sub-centimeter lesions lying at high SCDs.

Another innovative optimization approach would be to optimize the collimator to be of lower resolution and higher sensitivity and then to process the obtained image with depth-dependent spatial resolution recovery filters to restore the loss in resolution. These filters are mostly incorporated into the iterative reconstruction algorithms in SPECT imaging but were also successfully implemented for planar bone scanning and shown to improve the image quality [60].

Implementing both MC simulation approach and RSM together makes it possible to realistically model the patient and the parts of the camera at necessary levels of detail. Besides, DoE allows the optimization to be done at acceptable number of iterations by shortening the total necessary simulation time. Additionally, it is flexible and permits the use of the desired objective function according to the problem formulation of the optimization.

Furthermore, RSM can be implemented so as to include different collimator materials as well as hole shapes. This approach is also applicable to cameras comprising pixelated scintillators by applying a constraint so that the collimator holes match the pixels. However, the continuous crystal chosen in this study prevents formation of possible artifacts originating from misalignment of collimator hole and crystal pitches in case of pixelated crystals [61]. All in all, for the best performance, the collimator needs to be optimized separately for each camera in an application-specific manner.

The optimum levels of collimator parameters presented in this study are not expected to bring any manufacturability challenge considering production process. Besides, from a manufacturer point-of-view, this approach can serve as a decision support system, which means the manufacturer can evaluate different combinations of collimator dimensions and compare them in terms of manufacturability, cost and achievable lesion detectability by analyzing the iso-CNR contours given in Figure 2.7. This trade-off would result in a higher number of collimator options according to the preferences of the manufacturer.

In this study, we assumed a homogeneous activity distribution throughout the breast, since it was shown a non-preferential uptake of sestamibi by the adipose and glandular tissue [41]. For the realistic tissue uptake levels taken in this work and data acquisition time of 10 min, the total counts in our simulated images were below 175,000 stated in SNMMI breast scintigraphy protocol [42]. Although this count level is applicable for cameras with larger FoV [32] used in the clinics, it is not adequate for the particularly small FoV camera used in this study, which images only a portion of the breast phantom. On the other hand, the count densities in the simulated images were found to be compatible with those found in the literature [32, 62] and therefore suitable for breast scintigraphy.

The modeling of the patient can be done arbitrarily complex by incorporating body parts that include realistic inhomogeneities in anatomy and activity uptake. So, in future work, as the second part of the study, other organs in the torso will be added to the digital phantom to simulate the background radiation more realistically, since the effect of scatter was shown to be elevated when the lesion lies closer to the chest wall [63]. Additionally, it will be useful to integrate patient variations, such as lesion depth, lateral position of the lesion and the breast thickness into this particular problem to obtain a robust collimator design.

As a conclusion, the presented RSM-based collimator design approach allows the determination of optimum collimator parameters yielding the highest CNR for a specified worst case lesion. In our case, the CNR value has been considerably increased

when compared with other collimators. In a clinical setting, this should translate into better lesion detectability.

3. ASSESSMENT OF NEC RATE FOR A PET SCANNER USING MONTE CARLO SIMULATIONS AND RESPONSE SURFACE METHODOLOGY

3.1 Introduction

Ideally, the rate of true coincidence events is expected to be a perfect indicator for image quality. However, it is not, since it should be adjusted for the noise caused by the scatter and random events. For this reason, the NECR is used, which is a measure for statistical data quality that reflects the ability of the PET scanner to record true events relative to scattered and random coincidence events per unit time representing the effective count sensitivity of PET scanners. It takes the relative tradeoffs and the contribution of all true, scatter and random coincidences to image noise into consideration [4,5]. Strother *et al.* [6] and Yang and Peng [64] stated that NECR is dependent on the square of the SNR, a well accepted image quality metric. In addition to that, the square of mean detectability has been shown to be proportional to NEC density in model observer studies under ideal conditions for all lesion sizes and contrast ratios by *et al.* [65].

Although the NECR does not take the effect of reconstruction algorithm or the spatial resolution of the scanner into account, it was addressed as being a useful metric for image quality by Badawi and Dahlbom [66]. One way to improve the counting performance is to increase the geometric sensitivity of the scanner by retracting the interplane septa and therefore acquiring the data in 3D mode [67], the advantages of which are shown in brain imaging as well as in whole-body (WB) imaging [68–71]. In 3D mode, however, the number of scatter and random events are also elevated beside the wanted true coincidence events [72].

Most work concerning the statistical data quality in 3D WB PET imaging concentrated on finding the relationship of the activity and scanner settings with the NECR

on a one-variable-at-a-time basis but did not address the effect of interactions. One other concern is the efficiency of the assessment procedure since physical or simulation experiments are time consuming.

In the present study, we concentrated on studying the effect of the activity, LET and CTW, which strongly affect the true, random and scatter event rates and thereby the NECR in 3D PET imaging by making use of MC simulations and systematic design-of-experiments tools.

3.2 Background

3.2.1 Coincidence Detection in PET Imaging

Collimation of gamma rays is achieved via physical collimation in a gamma camera, however event detection relies on electronic collimation in PET imaging. An event is accepted as a valid coincidence only if two photons are detected within a predefined time window and if the energy deposited in the crystal is within the selected energy window. Additionally, line-of response formed by these two detected photons lies within a valid acceptance angle. However, there are also unwanted events, which are detected as a result of scattered photons or from unrelated positron annihilations [73] (Figure 3.1):

1. A *single event* is referred to a single photon counted by a detector. Only a portion of them can be converted into paired coincidence events (typically 1% to 10%).

2. A *true coincidence event* is a wanted event that derives from a single positron-electron annihilation. The two annihilation photons both reach detectors on opposing sides of the tomograph without losing much energy by interacting with surrounding atoms.

3. A *random coincidence* occurs when two nuclei decay at approximately at the

same time and two photons coming from different annihilation events are counted as coincidences since their detection fall within the coincidence time window, whereas the other two photons are lost. These events lead to inaccuracies in quantification in the final images and introduce additional statistical noise to the data.

4. *Multiple events* are similar to random events, except three photons from two annihilations are detected within the coincidence timing window. Since there is an ambiguity in deciding which pair of events arises from the same annihilation, these are rejected.

5. *Scattered events* happen when at least one of the photons coming from a single positron annihilation undergoes a Compton scattering prior to detection. Since Compton scattering causes a loss in energy of the photon and change in direction of the photon, the line-of-response assigned to the event is uncorrelated with the origin of the annihilation event. Therefore, scatter events cause decreased contrast and erroneous quantification of isotope concentrations in the final image.

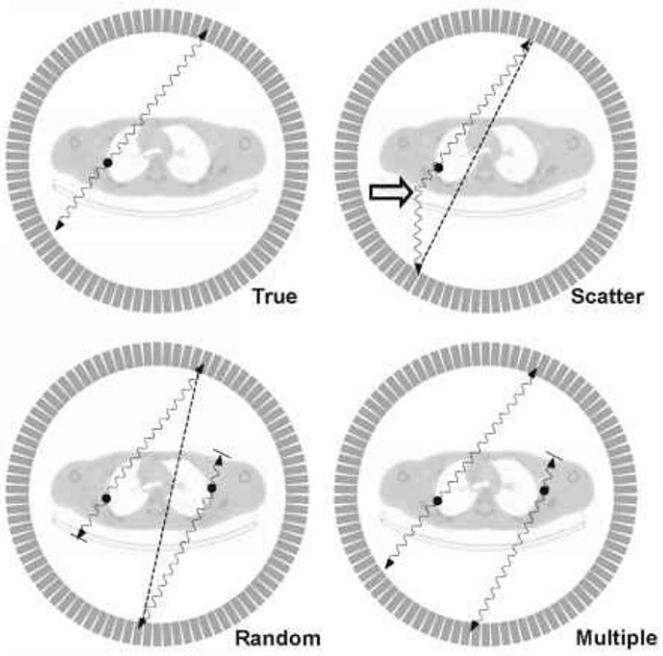


Figure 3.1 True, scatter, random and multiple events detected in PET imaging [73].

3.2.2 Overview: Data Acquisition and Event Processing Parameters Affecting Statistical Data Quality

The rate of true coincidences is proportional to the activity in the FoV, whereas the random coincidence rate (R) changes with the square of the activity in the FoV (1).

$$R = 2\,\tau\,N_1\,N_2 \tag{3.1}$$

where 2τ is the coincidence time window and N_1 and N_2 are the individual detection rates which are directly proportional to the activity in the FoV. The NECR was described as a metric for PET image and data quality and its dependence on the injected activity was demonstrated [74–79].

In PET imaging, only coincidence events depositing energy above a threshold value are accepted. Because of lack of interplanar septa in 3D PET imaging, the region of the energy spectrum lying between this threshold, namely the LET and the photopeak of 511 keV includes more Compton events compared to two-dimensional (2D) data acquisition (Figure 3.2). Therefore, with increasing LET the number of scattered coincidences in the acquired data is expected to decrease. In addition to that, the number of random coincidence events, covering a wide energy range, will also decrease. However, the number of true coincidences will also decrease with an increased LET, since some photons belonging to true coincidence events do not deposit all their energy inside the scintillation crystal when they interact with it via Compton scattering [74]. Thus, the rate was considered as a function of LET in previous studies [74,80–83]. Kohlmyer *et al.* [80] conducted a phantom study to investigate the effects of LET on NEC curves and contrast-to-noise ratio for positron volume imaging. Mawlawi *et al.* [83] reported the effect of LET on NEC rate and sensitivity where an optimum level for LET was investigated for 3D mode.

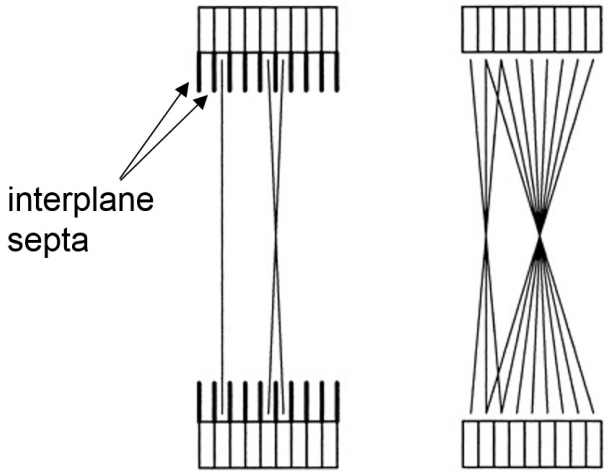


Figure 3.2 **a)** 2D and **b)** 3D data acquisition in PET [84].

Both the random and the true coincidence rate are functions of CTW which can be adjusted to further optimize the NEC rate [74]. Yang *et al.* optimized [81] the scanner settings for the best NEC rate performance taking the sensitivity trade-off into consideration. Another approach for optimizing the CTW is proposed by Conti [85] where a different time coincidence window is assigned to each line of response based on the CT attenuation map. Poon *et al.* [86] implemented a variable coincidence time window that is a function of ring difference to reduce the impact of randoms.

3.2.3 Relation between NECR and SNR

The formula for SNR was originally derived by Strother *et al.* [6] to relate the count rates of a PET scanner to SNR using NECR in 1990. Recently, the formula for SNR at the center of a uniform cylindrical phantom was shown by Yang and Peng [64] to be

$$SNR = K\pi^{-\frac{3}{4}}2^{\frac{3}{2}}s_v{}^{\frac{3}{2}}f_{corr}^{\frac{1}{2}}D^{-\frac{3}{2}}\left[\frac{T_t}{(1+f_s+f_r)}\right]^{\frac{1}{2}}. \tag{3.2}$$

where s_v is the image voxel size and D is the phantom diameter. Factor K depends on

the type of filters used in image reconstruction. f_s and f_r are the scatter and random fractions, respectively. T_t is the total true counts, whereas the term f_{corr} is the average attenuation and deadtime correction factor for a projection, which is assumed to be linear for a circular phantom.

Whereas, NECR is calculated as shown in Eq. 3.3.

$$NECR = \frac{T^2}{T + S + kR} \tag{3.3}$$

where T, S and R represent the true, scatter and random event rates, respectively. k is factor that is chosen according to the random estimation method. It is chosen to be 1 in case of noiseless estimation, whereas its value is set to 2 whenever the estimation is performed based on real-time random subtraction causing large variances. In this study, its value was taken as 1, since we assumed a noiseless random estimation using simulation data.

Based on Eq. 3.2 and Eq. 3.3, we can relate SNR to NECR as in Eq. 3.4.

$$SNR \propto \sqrt{NECR} \tag{3.4}$$

3.3 Materials and Methods

3.3.1 Model Description of the PET Scanner in GATE

In this study, we simulated the PET module of the GE Discovery LS PET/CT scanner, the model of which has been validated by Schmidtlein *et al.* [87] using GATE MC simulation package [88]. GATE is an open-source, Geant4-based [89] simulation platform developed by the international OpenGATE Collaboration [90] which is designed for NM (PET and SPECT), CT and radiation therapy applications includ-

ing well-validated physical models and geometry as well as event processing modeling tools [88]. The detailed workflow of GATE can be found in Appendix A.2.

The basic specifications of the simulated scanner were designed in agreement with the real tomograph. The 3D PET scanner model has 18 detection rings, each of which has 672 bismuth germanate (BGO) crystals making an overall total of 12,096 crystals. There are a total of 56 detector modules that are arranged in a ring. Each module is comprised of 6 detector blocks. The dimensions of each individual BGO crystal are modeled as 4 mm x 8 mm x 30 mm [87, 91, 92]. Moreover, the shielding and packing materials and the patient bed are also included in the digital model [87] (Figure 3.3).

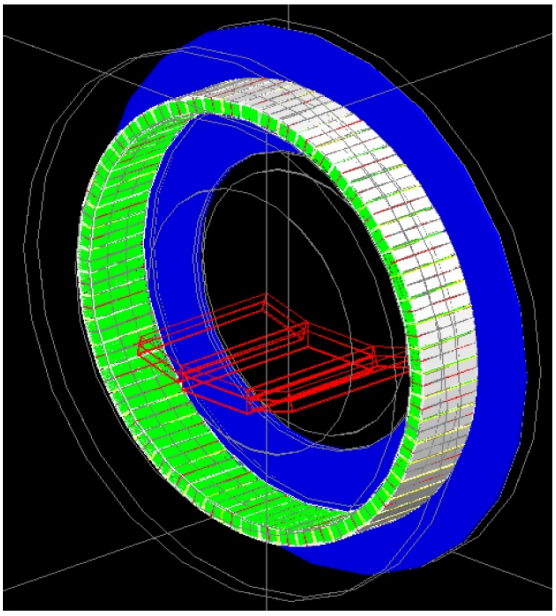


Figure 3.3 Geometry of GE Discovery LS PET module modeled using GATE simulation platform.

The event processing parameters were modeled via digitizer modules in GATE to simulate the trend of the experimental count rates published in [87] with increasing activity in the FoV. A singles trigger of 100 keV was applied to the signal. The energy resolution of the system was modeled as 20% at 511 keV and the lower and upper energy thresholds of 375 keV and 650 keV were implemented as in [93], respectively. Furthermore, paralyzable deadtimes were applied on the single events both at the

module and block levels. The time resolution of the system was modeled as 5 ns at full-width-at-half-maximum (FWHM) [94]. A time window of 12.5 ns and a minimum sector difference of 16 were applied to the coincidences as given in [93].

The output files were observed in ROOT [95] format which is a framework developed at CERN to enable the processing of large amounts of high energy physics data. A maximum ring difference of 11 was applied to fully 3D acquisition data via post processing following the data processing procedure described by [87].

3.3.2 Cluster Implementation of Simulations

GATE allows realistic description of geometries and simulations of sources, physical interactions and digitizer responses together with time management of detector movement and radioactive decays of sources. However, such accurate simulations come with an important disadvantage of need for high computational power and long computation times. One of the alternatives to overcome these issues is to parallelize the simulations on a computer cluster [96].

Therefore, we parallelized the simulations on a Linux computer cluster with 48 CPU capacity for each user on National Grid Initiative TR-Grid which is designed, built and coordinated by TUBITAK ULAKBIM High Performance and Grid Computing Center [97].

For this purpose, we implemented three steps to parallelize the simulations. These are job-splitting, running the simulations on 48 CPUs and file merging. The jobs were split using GATE in a time-domain decomposition scheme into smaller experiments of equal length using a random number generator providing statistically independent seeds. Finally, the outputs of individual parallelized simulations were merged using ROOT.

3.3.3 Evaluation of the Scatter Fraction and the Noise-Equivalent-Count Rate and Validation of the Scanner

Event rates and the derived NEC rates were determined according to the NEMA NU-2 2007 count-rate protocol [98], using a 70 cm long polyethylene NEMA count rate phantom of a radius of 10 cm with a line source of activity offset from the center by 4.5 cm. The cylindrical phantom was placed at the center of the axial and radial FOVs of the scanner. Data for the estimation of count rates were acquired for 5 s [99]. During the estimation of the count rates, the acquired sinograms were restricted to a circular FoV of radius of 12 cm the center of which is coincident with the center of the phantom, as stated in NEMA NU-2 protocol.

The simulated count rates were extracted from the ROOT output files using C++ scripts using its own compiler. NECR and the scatter fraction (SF) were then calculated based on these count rates using Eq. 3.3 and Eq. 3.5, respectively.

$$SF = \frac{S}{T + S} \tag{3.5}$$

3.3.4 Implementation of the Response Surface Methodology

A three-factor BBD (Appendix B.1) consisting of 17 experimental runs using the parameter ranges in Table 3.1 was employed including 5 replicates at the center point (Table 3.2). The activity range was chosen to lie between 109 MBq and 436 MBq, which is the range where the peak NECR was expected to be observed. LET was varied between relevant values of 375 keV and 475 keV, this range includes values encountered in the relevant literature. Finally, CTW was chosen to be between FWHM of the timing resolution of the scanner (5 ns) and the third multiple of it, covering relevant possible settings for this scanner.

Table 3.1
Design parameters and their experimental levels to model NECR.

Independent Variable	**Unit**	**Symbol**	**Level**		
			-1	0	1
Activity	MBq (kBq/ml)	A	109 (5)	272.5 (12.5)	436 (20)
Lower Energy Threshold	keV	B	375	425	475
Coincidence Time Window	ns	C	5	10	15

Table 3.2
Box-Behnken design of experiments.

Exp. #	**A Activity (MBq)**	**B LET (keV)**	**C CTW (ns)**
1	436.0 (1)	475 (1)	10 (0)
2	109.0 (-1)	475 (1)	10 (0)
3	272.5 (0)	425 (0)	10 (0)
4	436.0 (1)	375 (-1)	10 (0)
5	272.5 (0)	375 (-1)	5 (-1)
6	272.5 (0)	475 (1)	5 (-1)
7	272.5 (0)	475 (1)	15 (1)
8	272.5 (0)	425 (0)	10 (0)
9	436.0 (1)	425 (0)	5 (-1)
10	272.5 (0)	425 (0)	10 (0)
11	272.5 (0)	375 (-1)	15 (1)
12	272.5 (0)	425 (0)	10 (0)
13	272.5 (0)	425 (0)	10 (0)
14	109.0 (-1)	375 (-1)	10 (0)
15	109.0 (-1)	425 (0)	15 (1)
16	436.0 (1)	425 (0)	15 (1)
17	109.0 (-1)	425 (0)	5 (-1)

-1: Low level, 0: Mean level, 1: High Level

Experimental data were fitted to a second-order polynomial model Eq. B.3 and regression coefficients were obtained. Significance of the regression model, individual model coefficients and interaction between them were statistically analyzed performing ANOVA.

3.4 Results

3.4.1 Validation of Count Rate Simulations

Overall, trends in true, scatter, random and NEC count rates could be predicted very well. The maximum relative error observed was found to be around 9% at 5 kBq/mL (Figure 3.4). With GATE, we also predicted the increasing trend of the scatter fraction with increasing activity in the phantom. With the patient bed included in our simulations, using default scanner settings (375 keV LET and 12.5 ns CTW), the scatter fraction of the system was calculated according to the NEMA NU-2 2007 protocol and found to be 44.7% which was consistent with the experimental findings of New York Hospital published in [87].

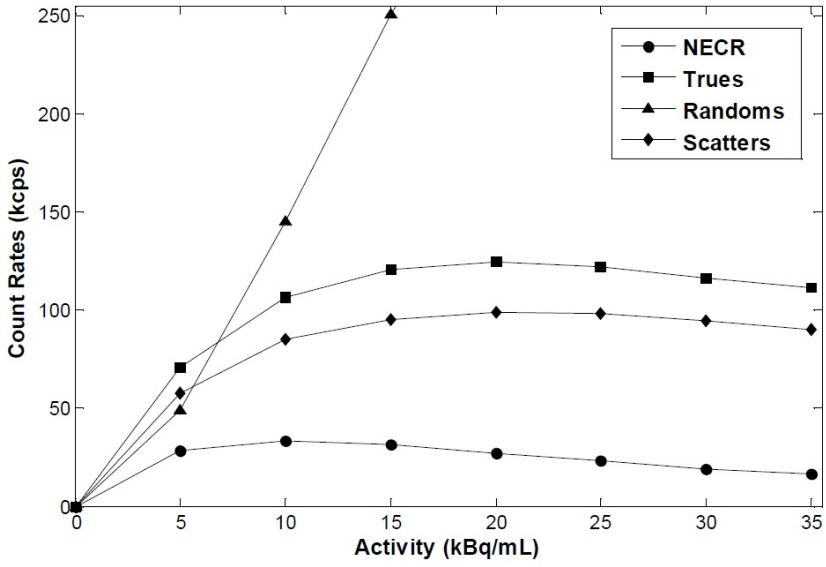


Figure 3.4 Simulated 3D count rate response of GE Discovery LS PET module.

3.4.2 Assessment of the Effect of Data Acquisition and Event Processing Parameters on Statistical Data Quality

The coded levels of the control variables were related to the NECR response via multiple regression equations to predict a quadratic polynomial model [38]. The fitted quadratic model (Eq. 3.6) was obtained performing a total of 17 simulations (Table 3.1). The cuboidal design of experiments and the corresponding NECR ranges are presented in Figure 3.5. According to the ANOVA analysis (Table 3.3), the fitted model adequately represented the NEC rates obtained from simulations. Moreover, ANOVA showed that a cubic model would not be bring any advantage to the model's predictive capability since it was found to be aliased.

$$\begin{aligned}\hat{Y} = 44.02 \; &+ \; 2.22\,A \; + \; 0.98\,B \; - \; 2.51\,C \; + \; ... \\ ... + \; &2.17\,AB \; - \; 3.40\,AC \; + \; 0.69\,BC \; + \; ... \\ ... - \; &6.02\,A^2 \; - \; 6.15\,B^2 \; - \; 4.97\,C^2\end{aligned} \tag{3.6}$$

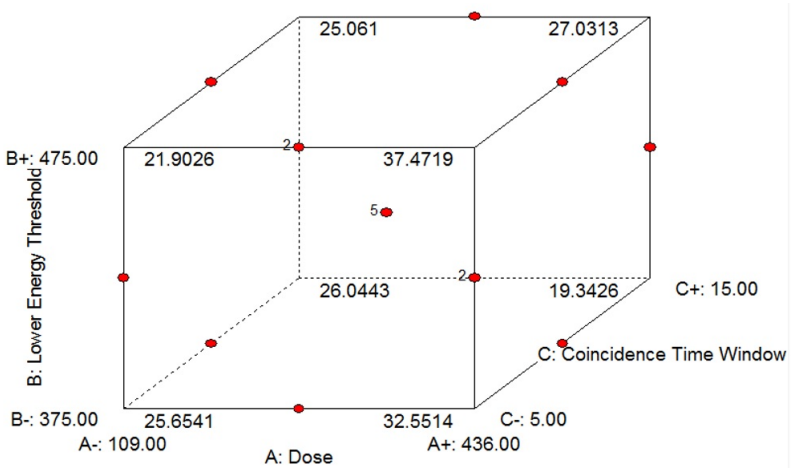


Figure 3.5 Box-Behnken design points shown in the 3D design space.

The significance of the model and the control variables was justified using R^2-values, F-values and significance probabilities. The results of the F-test showed that

the model was found to be significant ($p<0.001$) whereas the lack-of-fit of the model was not significant ($p=0.76$). The R^2-value value of the model was found to be 0.9771, whereas the predicted R^2 is 0.9861 which is in reasonable agreement with the adjusted R^2-value of 0.9935. R^2-values close to 1 indicated the adequacy of the model. A high predicted R^2-value is an indicator for the high predictive capability of the model. Moreover, since the adjusted R^2-value is an adjusted metric for the number of predictors of the model, its high value shows that the included models terms improve the model more than would be expected by chance. The data of the NEC rate predicted by RSM model were plotted against the corresponding experimental data of the NEC rate (Figure 3.6). It can be clearly seen that the predicted values of the NEC rate are in a good agreement with the actual values observed from simulations.

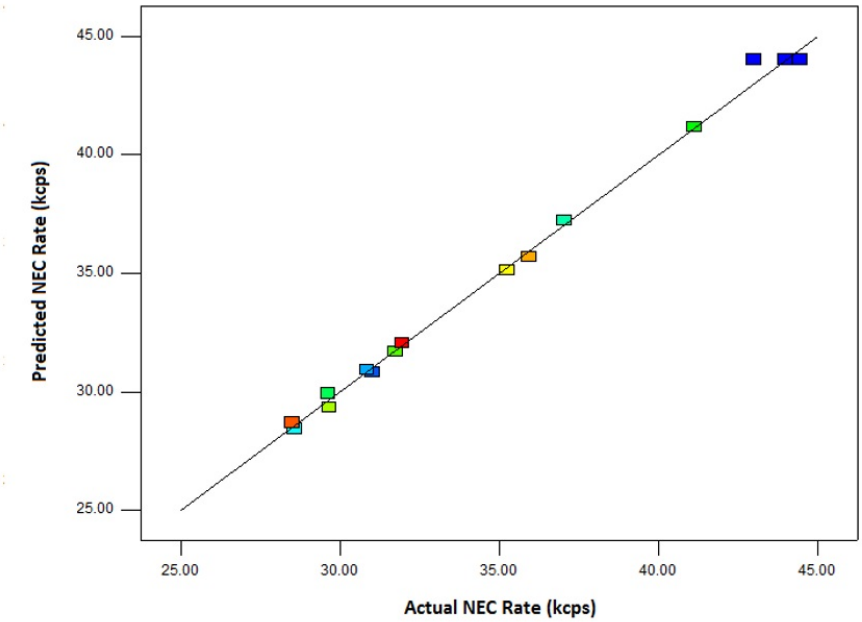


Figure 3.6 Predicted vs. simulated NECR.

The ANOVA results of the regression parameters of the predicted second-order response models for NECR showed that both linear (A, B, C) and quadratic parameters (A^2, B^2, C^2) and their interactions (AB, AC, BC) were highly significant with $p<0.05$ (Table 3.3).

Table 3.3
ANOVA results for quadratic response surface model.

Source	Sum of Squares	df	Mean Square	F Value	p-value Prob>F	
Model	628.64	9	69.85	271.41	<0.001	significant
A - Activity	39.32	1	39.32	152.78	<0.001	
B - Lower Energy Threshold	7.75	1	7.75	30.12	0.001	
C - Coincidence Time Window	50.51	1	50.51	196.25	<0.001	
AB	18.80	1	18.80	73.06	<0.001	
AC	46.23	1	46.23	179.65	<0.001	
BC	1.92	1	1.92	7.44	0.029	
A^2	152.40	1	152.40	592.19	<0.001	
B^2	159.29	1	159.29	618.98	<0.001	
C^2	104.09	1	104.09	404.47	<0.001	
Residual	1.80	7	0.26			
Lack of Fit	*0.41*	*3*	*0.14*	*0.39*	*0.76*	*not significant*
Pure Error	*1.39*	*4*	*0.35*			
Total	630.44	16				

The perturbation plot given in Figure 3.7 demonstrates the effect of the three parameters on the NEC rate providing an opportunity to observe the change in the NEC rate moving along each curve as LET and CTW deviate from their standard levels together with the effect of activity on NECR.

The predictive model (Eq. 3.6) shows that the activity and LET indicate linear effects that may increase the response whereas the negative one obtained for CTW tends to decrease it. Among the three parameters, CTW has the highest main effect on the NEC rate with a regression coefficient of -2.51 and is followed by the activity (2.22) and LET (0.98).

The quadratic components of independent variables LET, activity and CTW demonstrate negative effects in descending order with coefficients -6.15, -6.02 and -

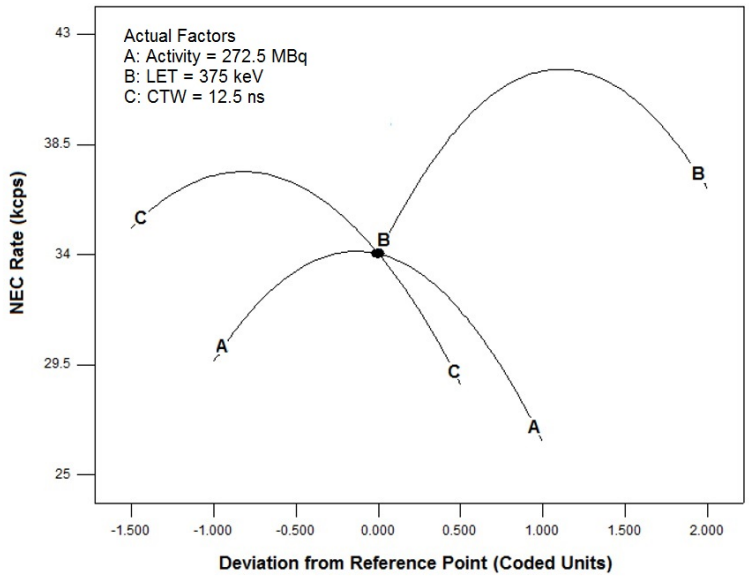


Figure 3.7 Perturbation plot of scanning parameters for NECR. At the point of intersection, the scanner parameters are kept at their default values (375 keV and 12.5 ns) and the activity is taken as 272.5 MBq. Individual effect and combined effects of parameters can be seen moving along the curves.

4.97, respectively. Negative coefficients for quadratic main effects imply a decrease in NECR when their values move away from their mean (0) levels. Thus, too much increase in activity causes pile-ups and setting the LET to higher values causes rejection of true events resulting in lower NEC rates. Furthermore, a wide CTW would accept too many random events, therefore is expected to lead to a significant decrease in NECR. On the other hand, at low doses and for narrower CTWs, the number of true events will decrease, while a lower LET results in elevated number of scatters, which will cause NECR to decrease.

Considering the interaction effects, the interaction activity*CTW has the strongest impact (-3.40), while the interactions of activity*LET and LET*CTW follow it with coefficients 2.17 and 0.69, respectively. Contour plots of the NECR examining the main interaction effects are shown in Figure 3.8. The plots are drawn according to the fitted model (Eq. 3.6) with respect to two parameters keeping the third constant each time. Figure 3.8a shows that higher activities in the FoV necessitate higher LETs to reach a higher NEC rate to eliminate scatter events. From the interaction graph of the activity and CTW (Figure 3.8b), it can be seen that increasing the activity, requires lower CTW

settings to overcome random coincidences. The interaction between LET and CTW is shown in Figure 3.8c which is found to be the weakest among all, that is evident from the circular shape of the contours rather than elliptical form.

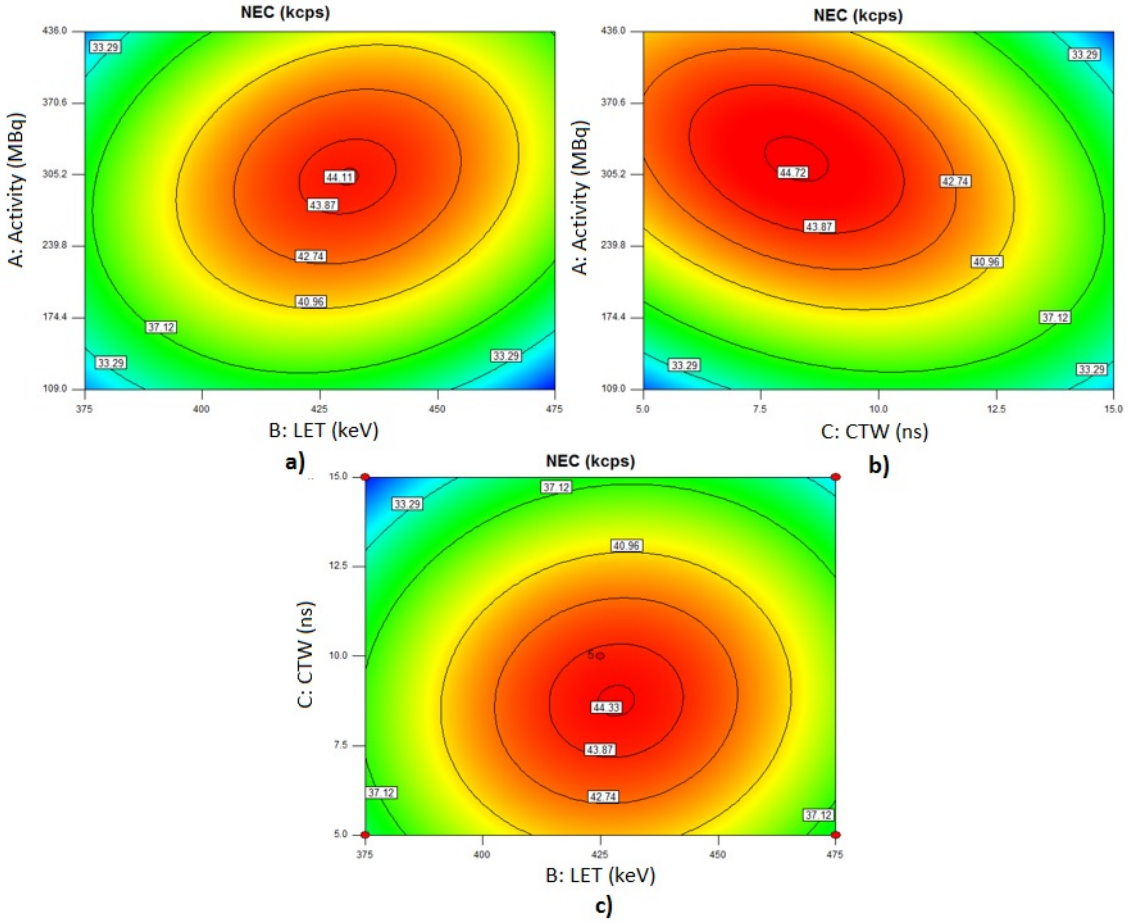


Figure 3.8 Response surface plot of NECR with respect to scanning parameters. **a)** Activity and lower energy threshold, **b)** activity and coincidence time window and **c)** lower energy threshold vs. coincidence time window.

3.5 Discussion and Conclusion

As observed in the regression analysis, CTW has the most significant linear effect on NECR. A wide CTW enables maximization of the sensitivity, but on the other hand it also increases the random rate. In addition, an elevated number of random and scatter events are observed since the phantom of a length of 70 cm extends beyond the

axial FoV and events coming from outside the FoV cannot be shielded completely. LET was observed to be the least strong linear factor on the NECR for the considered range of values in this study. The evidence of presence of interaction among parameters makes this approach superior compared to one-variable-at-a-time assessment techniques.

Considering organ-specific imaging, Peng [100] presented a MC simulation study where the researcher investigated the feasibility of building a cardiac-dedicated PET system that uses lutetium-yttrium oxyorthosilicate (LYSO) crystals with depth of interaction (DoI) and time-of-flight (TOF) capabilities. In this study, Peng also studied the effect of LET and CTW on NECR for values between 6-48% and 1-12 ns, respectively, over a wide of range activities. The combined effect of these parameters can be efficiently and statistically examined using response surface methodology.

The breast specific PET scanner developed by Miyake *et al.* [101] makes use of lutetium gadolinium oxyorthosilicate (LGSO) crystals which has a far more shorter decay time (40 ns) compared to BGO. Based on this fact, CTW could be reduced to 4.5 ns to reduce the random rate and obtain a high NECR. Nevertheless, the researchers mentioned the necessity for further investigation for optimum LET and CTW values in their work, so that the peak NECR could be further increased. This fact demonstrates the need for studying the effect of these parameters on NECR to optimize those and the applicability of the proposed method to breast-specific small-bore positron emission mammography scanners in addition to large-bore cameras.

Furthermore, there are also studies where a variable coincidence time window is suggested for small-animal PET imaging [102, 103]. Cooper [102] also mentioned the need for examining the effect of CTW on the performance so that the timing resolution will be optimized. Others, such as Wang *et al.* [104] examined the influence of the energy window on the effect of NECR and scatter fraction for both rat and mouse phantoms. Therefore, small animal PET imaging is another potential field where the method presented in this study can be implemented with an addition of animal size as a new variable.

Moreover, commercial PET scanners have a fixed coincidence window, however there may be cases where CTW can be shortened for some patients, especially smaller patients, and/or when performing brain imaging, for the sake of better discrimination between true and random events [105]. Therefore, realistic phantom experiments or simulations should be conducted to decide for optimal data acquisition and event processing parameters. However, since the length of CTW effects scanner calibrations such as normalization and standardized uptake value (SUV), the scanner has to be calibrated for each CTW value before these experiments. Yet, the calibration routine is very time-consumptive, typically taking at least 11 hours for each coincidence window [105]. Thus, efficient experiment designs to investigate the response of the system for different patient and acquisition types is crucial and the use of MC simulations will be even more beneficial with the use of computer clusters considering time constraints. Moreover, for a patient-based optimization of scanning parameters, it gets even more complicated to build a model for the NECR response as the number of variables increase, such as patient variations, even though the time for PET calibration for varying time windows can be decreased by the method suggested by Laurence and Kolthammer [105]. Additionally, it will not be possible to obtain the real optimal CTW value without knowing the interactions between the parameters, as we have shown in this study.

There are also studies where various other approaches were suggested for the sake of reducing the number of random events. One method implemented for this purpose in TOF scanners is the use of a truncated time window that is smaller than the actual window to restrict the TOF bins to objects that are smaller in size compared to the actual object imaged. Another technique makes use of the patient's CT morphological data to adjust the coincidence time window [106]. In this TOF masking approach, events localized as coming from outside the patient are assumed to be randoms without taking the statistical uncertainty in timing into account. This causes rejection of true events besides randoms. A third method implemented in a scanner with a longer axial FoV is to adjust the window according to the ring difference [86]. There are also other studies where an adjustable coincidence window is chosen between different pairs of detector modules or locations of sinogram radial bins are used to reject LORs located

outside of the FoV. However, since these do not take the timing resolution into account, the number of true coincidences are again reduced [106]. All of these methods require an investigation of the effect of the coincidence time on the scanner's data quality while taking statistical uncertainties, patient variations and length of LORs into account.

In [107], Schug *et al.* suggested a narrower or wider energy window to obtain a better timing performance or a higher sensitivity, respectively. Besides, they proposed a sliding coincidence window that is varied depending on the activity for the PET scanner with a TOF-capable PET/MRI insert they investigated. They propose a sequential implementation of energy and coincidence windows to the data. The overall effect of changing both of these parameters can be realistically examined by making use of RSM and MC simulations paving the way for obtaining the real optimums for these parameters for different objectives and data acquisition conditions.

It is also worthy to note the potential usage of BGO crystal in state-of-the-art and future PET scanners because of its very low intrinsic radioactivity in case of low activity sources [108]. In this respect, BGO has an advantage over lutetium oxyorthosilicate (LSO) or LYSO crystals since its intrinsic prompt counting rates were found to be nearly 10^3 times lower [108]. Furthermore, Efthimiou *et al.* [109] showed that presence of intrinsic radioactivity in the crystal affects timing performance by affecting the dead time of the detectors and thereby singles, trues, and randoms count rates. These facts make BGO still a good candidate for studies where there is no need for TOF information or for imaging low-dose sources with the development of application- and target-specific radiopharmaceuticals.

To conclude, the presented approach was found to be very benefial for examining the effect of event processing parameters and their interactions on NECR, since a high degree of interaction between them was found. Therefore, the prediction of optimum values would be difficult, which is crucial to obtain a good statistical quality in counts that is expected to translate in better lesion detectability in a clinical setting. From a manufacturer point-of-view, this approach can be of high potential for optimization of data acquisition and event processing parameters for newly developed scanners.

4. OVERALL CONCLUSIONS

Molecular nuclear medicine involves non-invasive imaging of human or small-animal (preclinical) physiological functions for oncology, neurology and cardiology. Besides, it contributes to the understanding of causes and pathways of diseases, treatment planning and monitoring of its effectiveness. An advantage of nuclear medicine over anatomical imaging modalities, such as CT, MR and US, arises from the fact that metabolic changes at cellular level occur prior to changes in anatomy [110]. To be able to further increase the diagnostic value of NM modalities, there is ongoing research for development new radiopharmaceuticals, as well as new software and hardware. This includes development of algorithms regarding data correction and reconstruction, design of application- and camera-specific collimators, preclinical, organ-specific and hybrid cameras, in addition to PET scanners with TOF capability, where effort is put on maximizing performance metrics related to image quality.

In this thesis, CNR was chosen as the measure of lesion detectability for the chosen gamma camera, since it is a metric capable of encompassing both the resolution and the sensitivity. On the other hand, the statistical data quality of the PET scanner was evaluated by NECR, because it represents the ratio of recorded true events relative to unwanted coincidences, namely the effective count sensitivity.

In the first study presented in this thesis, a breast-specific gamma camera design was taken as a case study in order to demonstrate the improvement achieved in CNR value when hole diameter, septal thickness and hole length of a parallel-hole hexagonal lead collimator was optimized. This study demonstrated that the pairwise interaction effects of the collimator parameters play a key role in determining the set of design parameter combinations that yield the highest CNR. Moreover, the behavior of the optimizer was investigated as the SCD of a lesion of fixed size and TBR is changed. Our findings revealed that the optimizer adapts itself to the spatial resolution/sensitivity trade-off as the lesion depth changes. In future work, realistic inhomogeneities in

anatomy and activity uptake as well as other organs in the torso and patient variations can also be incorporated into this particular optimization problem. Moreover, this proposed method is also applicable to other detector configurations, such as the ones using pixelated crystals or other types of collimators of different geometries or made of other materials. Based on our results and potential extent of use, we conclude that the advantages obtained with this method may lead to an advancement in the state of the art in collimator design.

The second study, on the other hand, concentrates on studying the effect of the activity, the lower energy threshold (LET) and the coincidence time window (CTW) on the NECR of a PET scanner for 3D imaging. Our findings showed that both LET and CTW showed significant linear and quadratic effects over a wide range of activity values. Moreover, presence of statistically significant pairwise interaction effects of the parameters on NECR proves that this procedure is superior in comparison to conventional one-variable-at-a-time assessment techniques. It is crucial to obtain a good model of statistical significance with respect to data acquisition and event processing parameters, since it would lead to realistic optimum values to maximize NECR and therefore into better lesion detectability in a clinical setting. Additionally, a thorough literature survey exhibited that the employed approach is also appropriate to be used for organ-specific, small-animal and TOF PET imaging.

APPENDIX A. Monte Carlo Tools in Nuclear Molecular Imaging

The Monte Carlo method is a numerical approach to simulate complex processes using statistical methods. The physical processes are modeled based on known probability density functions (PDFs) using uniformly distributed random numbers.

Since this technique was first implemented to scintillation camera by Anger and Davis in early 60's [111] to calculate the intrinsic efficiency and the intrinsic spatial resolution for NaI(Tl) crystals of varying thicknesses for different photon energies [112], it gained a great interest for modeling physical processes in medical imaging where analytical or experimental approaches are not applicable or they cannot be easily implemented [113].

In a MC simulation of a NM scanner, the scanner is described with the physical characteristics of the real system. The particle and photon trajectories and interactions are simulated by using PDFs. The response of the simulated system converges to the average behavior of the real system and therefore is more reliable if the experimental uncertainty is decreased by increasing the number of events [112, 114].

MC simulation is a very useful tool for NM imaging since it can be utilized for various purposes, such as to investigate the effect of parameters that are impossible to measure experimentally, building and optimizing new scanner configurations and developing new correction or reconstruction algorithms.

There are two types of MC codes that can be used to simulate NM imaging systems:

1. General purpose: Programs, such as EGS4 [115], MCNP [116], ITS [117], and GEANT4 (GEometry ANd Tracking 4) [89], have mainly been developed for high

energy physics and dosimetry to simulate particle transportation and cross-section up to several GeV energies.

2. Dedicated to NM: Programs that have been designed specifically to solve problems for imaging applications are SIMIND [39,47], PETSIM [118], PET-SORTEO [119] and GATE [88], and SimSET [120].

In this thesis, we made use of SIMIND and GATE programs, the details of which were summarized below:

A.1 SIMIND

SIMIND is a well-established MC code that has been widely used for 30 years [39,47]. It is capable of simulating nuclear scintillation detectors for stationary as well as tomographic imaging (SPECT only). Its code is written in FORTRAN-90 and has versions for widely used operating system platforms. All physics interactions, source and phantom geometries, simplistic or anthropomorphic, and various materials can be simulated realistically using SIMIND. Simulation of different collimators of various shapes and sizes permits studies on spatial resolution and sensitivity [39,121].

The SIMIND system consists of two main programs, namely the CHANGE program and the SIMIND simulation program. The CHANGE program (Figure A.1) serves as an interface to define the necessary simulation parameters for the system being simulated which then will be taken as inputs by the SIMIND simulation program.

It also contains several simulation flags to manage certain types of simulation features, such as SPECT simulation, transmission imaging, the inclusion of a collimator, simulation of photon interaction within the phantom or cover, etc. (Figure A.2) Whenever the definition of simulation parameters is finished, the SIMIND program performs the actual simulations. Finally, SIMIND writes the output of the simulations, such as the observed energy spectrum and projection images to external files [47].

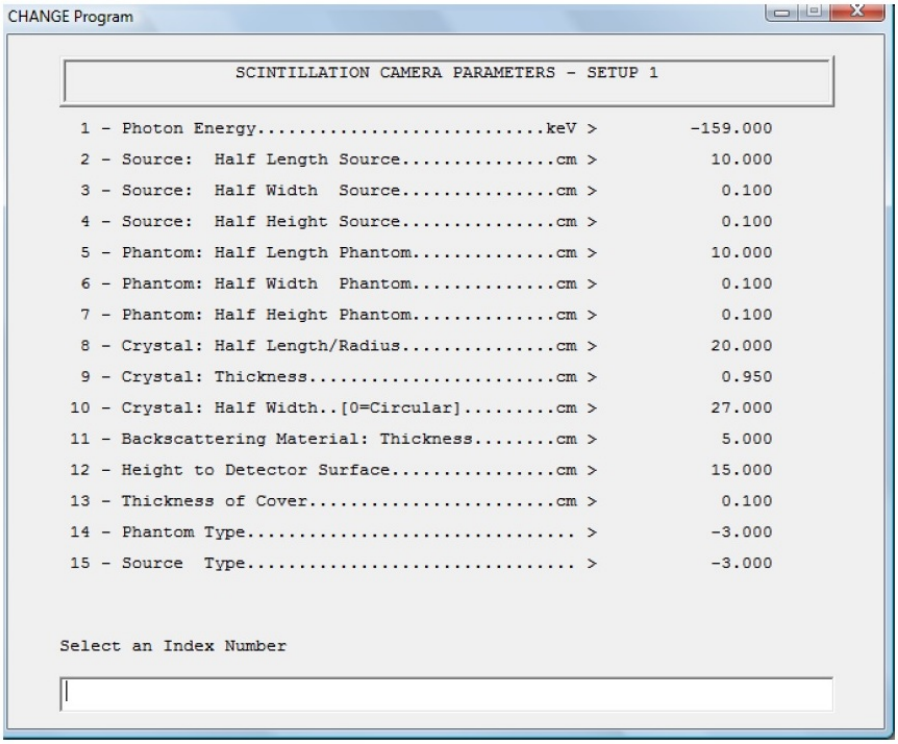


Figure A.1 Interface of the CHANGE program [47].

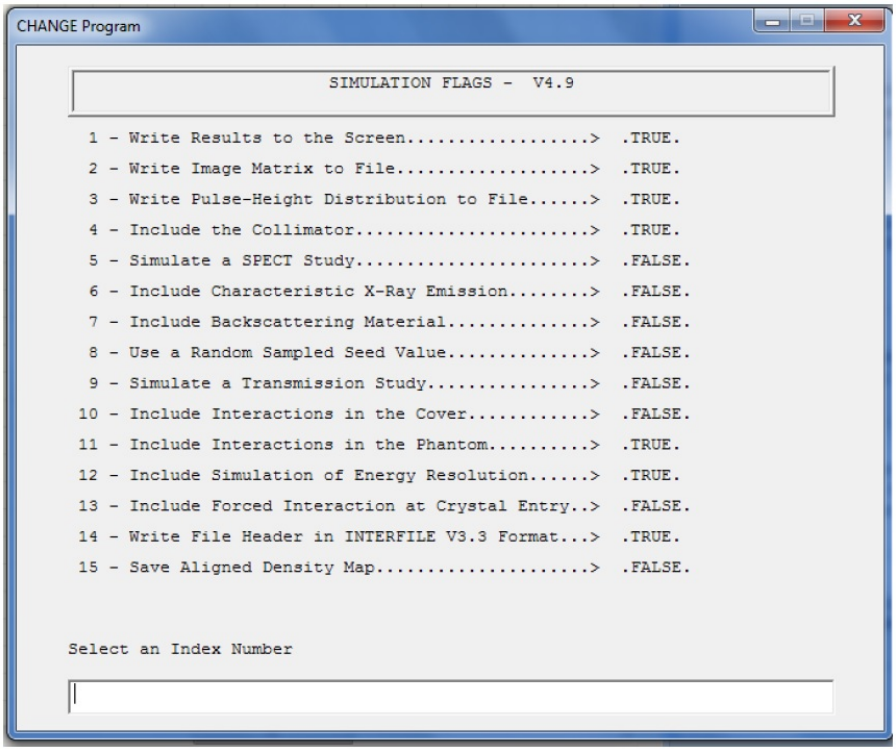


Figure A.2 Simulation flags within the CHANGE program [47].

A.2 GATE (Geant4 Application for Tomographic Emission)

A large number of validation studies have been proposed for usage of GEANT4 in medical studies, including validation of radiotherapy, electromagnetic and nuclear interactions and proton therapy applications [122–125]. Despite all the abilities of GEANT4, it is not capable of handling decay kinetics, dead time and movements, for instance patient, respiratory and cardiac motion or scanner rotation. Therefore, a new dedicated toolkit for tomographic emission, GATE (GEANT4 Application for Emission Tomography), was developed by the international OpenGATE collaboration [90] and is dedicated to numerical simulations in medical imaging and radiotherapy [88].

It currently supports simulations of PET, SPECT, CT and Radiotherapy experiments [126]. GATE uses GEANT4's libraries to simulate particle transport. It makes use of an easy scripting language allowing configuring simulations such that the user does not need to be familiar with C++ programming. The program has a layered architecture with a core layer close to GEANT4 kernel that manages the main tools and features of GATE, such as time, geometry, and radioactive sources, an application layer with C++ base classes and a user layer where the simulations are set up using command based scripts.

A.2.1 Simulation architecture

Typical steps of a GATE simulation are described below [90]:

1. The user decides on the verbosity level and visualization options.

2. The geometries of different imaging systems and phantoms are defined starting from the dimensions of "world", the environment for the simulation to take place. Various predefined templates of imaging systems, such as "scanner", "SPECTHead", "cylindricalPET", "ecat", "CPET", "OPET" and "OpticalSystem", are available in GATE, which can be used to simulate the existing scanners.

3. The digitizer module defines the detection parameters to simulate the behavior of the detectors and signal processing chain, namely the electronic readout scheme of a scanner. Digitizer parameters include energy and timing resolution, as well as energy thresholds, timing parameters and dead-time in detectors.

4. The user decides the physical processes for the simulation. This performed by using the packages available to simulate electromagnetic processes based on GEANT4; these are the standard energy package, the low energy package and the PENELOPE package. Standard processes are effective between 1 keV and 100 TeV. Whereas, the low energy package models photon and electron interaction down to 250 eV and includes Rayleigh scatter and provides more accurate models for medical application. Additionally, the PENELOPE processes define interactions between 250 eV and 1 TeV.

5. The radioactive source is defined by modeling its type, activity and half-life ($t_{1/2}$), source geometry, emission angle, position and movement. In addition to simple phantoms having standard geometries, parameterized ones can also be defined where the voxels that can be varied in size, shape and material. These voxelized phantoms or patient data can be used as inhomogeneous anthropomorphic attenuation maps or emission sources so as to simulate realistic acquisitions.

6. The output format is chosen by the user according to the simulated scanner and the needs of data processing. The available output formats are ASCII, ROOT, Interfile, LMF, and ECAT. The ASCII format gives all information about the detected photons in a large text file allowing the user to process the raw data in a flexible manner. However, since ASCII files are not compressed, the output files become very large. The ROOT format developed at CERN [95], which has been used in this study, is very powerful since it provides event-by-event characteristics for coincidences, hits and singles for a PET simulation. The data format is structured to be tree-shaped and the necessary information can be extracted with macro files written in C++ within ROOT. The Interfile format is especially suited for acquisition protocol using a multiple headed rotating gamma camera. Lastly, the sinogram and LMF outputs are available for "ECAT" and "cylindricalPET" systems, respectively.

7. Data acquisition is started.

A.2.2 Parallelization of simulations

GATE allows the user to realistically describe the geometries and sources, physical interactions and detector responses. Additionally, GATE provides accurate detector movement and time management of physical phenomena. However, this can be achieved at the expense of long computation times. Based on this fact, one approach to shorten the overall simulation time is to parallelize of simulations on a computer cluster. The studies have shown that GATE simulations can be scaled very well on a cluster of homogeneous computers [96, 127].

Three steps to parallelize simulations are job-splitting, running the simulations on a number of CPUs assigned by the user and file merging.

The simplest job-splitting approach is to split the simulation into smaller experiments of equal length by using virtual time slices. For this purpose, the job splitter provides a specific submit file for the supported cluster platforms to launch the simulations. The currently supported cluster platforms are openMosix, openPBS, Condor and Xgrid. For job-splitting, the chosen random number generator provides statistically independent seeds for the fully resolved, non-parametrized individual macro-files.

The outputs of individual parallelized simulations are obtained in ROOT format which will be then used by the file-merger to get the final output of the simulation without any user interaction. For this purpose, a split file is generated that contains all information about the partitioned simulation to facilitate the merging of the output files. The obtained output file can then be used as a usual single CPU output file [128].

APPENDIX B. Principles of Response Surface Methodology

RSM was introduced by Box and Wilson in 1951 [7] to tackle design optimization problems where it is complicated or impossible to derive analytical models. RSM is based on the theory of DoE and allows systematic optimization of complex systems using a successive modeling approach. This methodology offers an appreciable advantage over one-variable-at-a-time optimization techniques since it also takes parameter interactions into account [38] and reduces the cost of expensive analysis methods and their associated numerical noise [129]. Therefore, RSM has been successfully implemented in various industries.

B.1 Sequential Workflow of RSM and Design of Experiments

RSM serves the purpose of developing an empirical relationship between a response of interest, y, and a number of associated independent variables $x_1, x_2, ..., x_k$ using a collection of mathematical and statistical techniques. Thus, this relationship is approximated by fitting a low-degree polynomial model (Eq. B.1).

$$y = f(x) + \varepsilon \tag{B.1}$$

where $f(x)$ is a function of powers and cross-products of powers of variables $x_1, x_2, ..., x_k$ up to a degree d (≥ 1) and ε is a random experimental error or common cause variation assumed to have a normal distribution with zero mean. Assuming that the model is an adequate representative of the response, the quantity $E(y)$ represents the mean response of y [51].

In most of the RSM experiments, the variables are transformed into coded variables, so that each has a zero mean and the same standard deviation which are usually defined dimensionless [130].

The first special case of model Eq. B.1 is the first-degree model which includes the main effects (Eq. B.2). Generally, the first order model is expected to be quite sufficient to approach the region for optimum conditions. The most frequently encountered first-order designs are 2^k factorial [131], Plackett-Burman [132] and simplex [133, 134] designs.

$$y = \beta_0 + \sum_{i=1}^{n} \beta_i x_i + \varepsilon \tag{B.2}$$

where n is the number of the independent variables, x_i, and x_j are the independent variables and β_0 and β_i are the regression coefficients for intercept and linear interaction terms, respectively.

As the experimental region moves near the region of optimum conditions, interaction terms ($\beta_{ij} x_i x_j$) are added to the main effects to be able to represent some curvature in the response function. In the case the curvature of the response cannot be modeled sufficiently, then the complete second-order model Eq. B.3 is utilized which is the second special case of Eq. B.1 [38].

$$y = \beta_0 + \sum_{i=1}^{n} \beta_i x_i + \sum \sum_{i<j} \beta_{ij} x_i x_j + \sum_{i=1}^{n} \beta_{ii} x_i^2 + \varepsilon, \tag{B.3}$$

where β_{ii}, and β_{jj} are the regression coefficients for quadratic and interaction terms in addition to Eq. B.2, respectively [51].

The most commonly used second-order designs are 3^k factorial [131], central composite [7], and the Box-Behnken designs [53]:

3^k factorial design consists all possible combinations of three levels of the k control variables (Figure B.1a). Based on this fact, this design loses its efficiency in the modeling of quadratic functions with a large number of variables. Fractions of a 3^k design can reduce the cost of running experiments based on this design [51].

The central composite design (CCD), introduced by Box and Wilson [7], projects the sequential nature of RSM in starting with a first order 2^k factorial design followed by the addition of 2k axial points and n_0 center point replications to fit a second order model. The 2k design points are arranged on the axis of each control variable such that two points lie at a distance of $-\alpha$ or $+\alpha$ from the design center (Figure B.1b). The value for α and n_0 chosen by the experimenter such that the design can possess certain desirable properties such that rotatability or orthogonality [51]. The three types of CCD are circumscribed, inscribed, and face centered.

The third design is the Box-Behnken design which was developed in 1960. BBD is based on the construction balanced incomplete block designs [53]. It is an efficient alternative to the CCD for a small number of factors (≤ 4) since it requires fewer experimental runs. Based on the fact that it is economical, this design is often preferred in industrial research processes [51]. BBD is a spherical design since it uses all the edge points of the cube each of which lies at a distance of $\sqrt{2}$ from the center design (Figure B.1c). Because of the spherical nature of BBD and the fact that it is rotatable or near-rotatable, the use of three to five center runs (n_0) are recommended. Since the design points of BBD does not cover the entire cube, it is not cuboidal. This fact restricts the use of BBD to the situations when the researchers are not interested in predicting response at the extrema, namely at the corners of the cube [38].

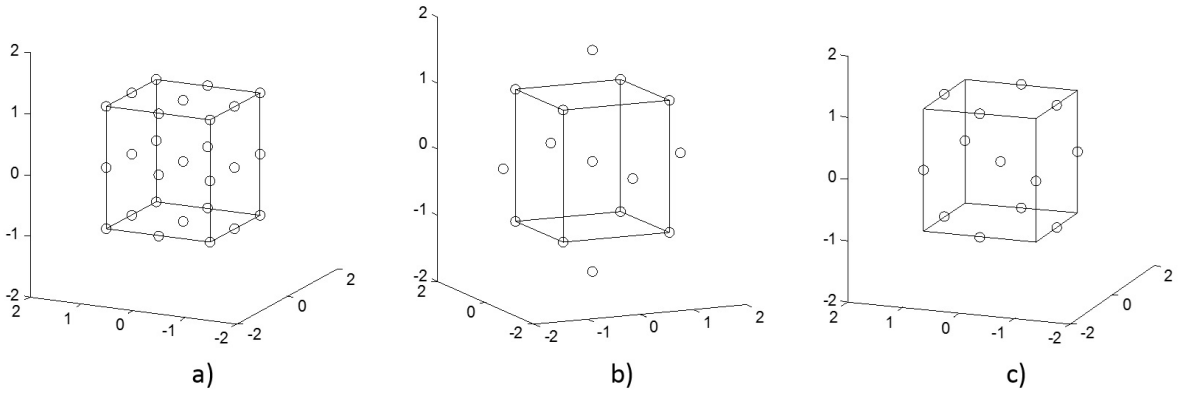


Figure B.1 Second-order experiment designs. **a)** 3^k factorial, **b)** CCD, and **c)** BBD.

B.2 Optimization of the Response

B.2.1 Analytical Approach

The analytical approach is the most straightforward technique to find the stationary points of the response surface, the second-order model of which is known to the experimenter. The steps of the analytical approach are given below [38]:

Consider the response surface model in Eq. B.3 in matrix form:

$$\hat{y} = b_0 + \mathbf{x}'\mathbf{b} + \mathbf{x}'\hat{\mathbf{B}}\mathbf{x} \tag{B.4}$$

where b_0, $\mathbf{b}$ and $\hat{\mathbf{B}}$ are the estimated intercept, linear and second-order model coefficients, respectively. Additionally, $\mathbf{x}' = [x_1, x_2, ..., x_k]$, $\mathbf{b}' = [b_1, b_2, ..., b_k]$ and $\hat{\mathbf{B}}$ is a k x k symmetric matrix, such that

$$\hat{\mathbf{B}} = \begin{bmatrix} b_{11} & b_{12}/2 & ... & b_{1k}/2 \\ & b_{22} & ... & b_{2k}/2 \\ & & \ddots & \vdots \\ sym. & & & b_{kk} \end{bmatrix}. \tag{B.5}$$

The location of the stationary point can be found by differentiating Eq. B.4 with respect to $\mathbf{x}$.

$$\frac{\partial \hat{y}}{\partial \mathbf{x}} = \mathbf{b} + 2\hat{\mathbf{B}}\mathbf{x} \tag{B.6}$$

Setting Eq. B.6 to $\mathbf{0}$, the stationary point of the system can be found as

$$\mathbf{x}_s = -\frac{1}{2}\hat{\mathbf{B}}^{-1}\mathbf{b} \tag{B.7}$$

Subsequently, the nature of stationary points can be determined by the canonical analysis; they will either be characterized as a stationary point yielding the maximum or minimum response or as a saddle point (Figure B.2) according to the signs of the eigenvalues $[\lambda_1, \lambda_2, ..., \lambda_k]$ of matrix $\hat{\mathbf{B}}$ [38]:

(1) If $[\lambda_1, \lambda_2, ..., \lambda_k]$ are all negative, the stationary point will yield the maximum response.
(2) If $[\lambda_1, \lambda_2, ..., \lambda_k]$ are all positive, the stationary point will yield the minimum response.
(3) If $[\lambda_1, \lambda_2, ..., \lambda_k]$ have mixed signs, the stationary point will be a saddle point.

In case when the stationary point is of no value, e.g. it is a saddle point, a useful procedure for localizing a point of maximum (or minimum) is the *ridge analysis*, a constrained optimization algorithm, which was first introduced by Hoerl [135] and later formalized by Draper [136]. Ridge analysis can be described as steepest ascent (descent) implemented to a second-order model [38], which optimizes the response $\hat{y}(\mathbf{x})$ on concentric hyperspheres of radius r (Eq. B.8) within the region R, therefore needs a rotatable design to fit the model to keep the prediction variance constant on the surface of any given hypersphere [51].

$$\sum_{i=1}^{n} x_i^2 = r^2 \tag{B.8}$$

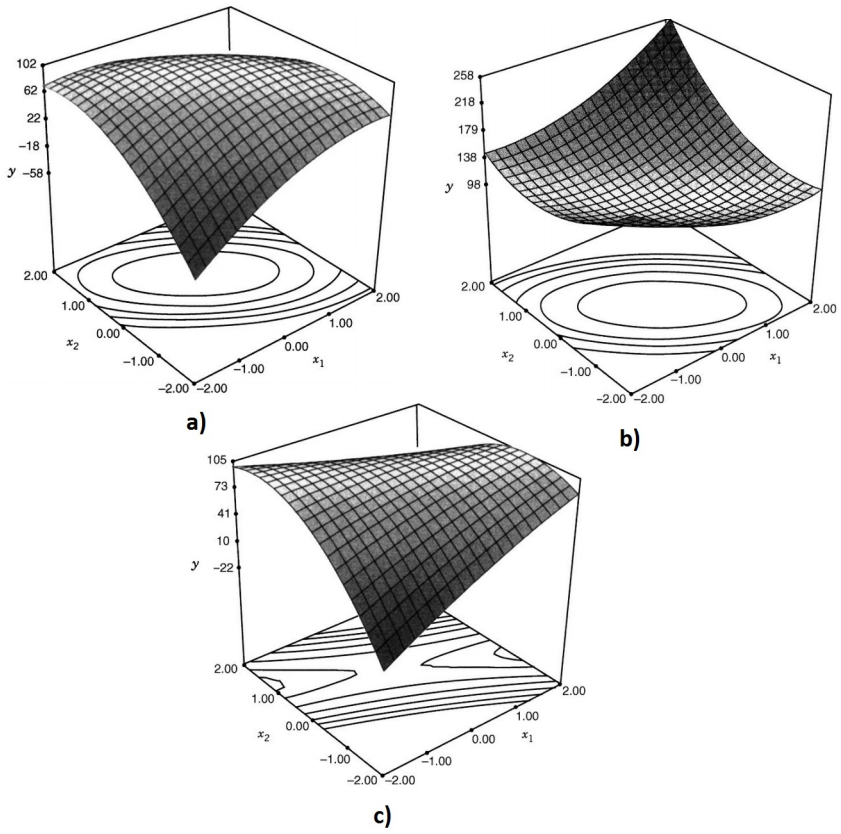


Figure B.2 Response surface of a second-order system displaying **a)** a maximum, **b)** a minimum, and **c)** a saddle point [38].

Therefore, using Lagrange multipliers, the constrained function to be optimized can now be written as

$$L = b_0 + \mathbf{x}'\mathbf{b} + \mathbf{x}'\hat{\mathbf{B}}\mathbf{x} - \lambda(\mathbf{x}'\mathbf{x} - \mathbf{r}^2) \tag{B.9}$$

Differentiating Eq. B.9 with respect to $\mathbf{x}$ and setting it equal to $\mathbf{0}$, we can solve for $\mathbf{x}$ and we obtain the stationary point

$$\mathbf{x}_s = -\frac{1}{2}(\hat{\mathbf{B}} - \lambda\mathbf{I_n})^{-1}\mathbf{b}. \tag{B.10}$$

A maximum (or minimum) will be obtained at this point if the second-order partial derivatives of L, or the Hessian matrix, will be negative definite (or positive definite).

$$\frac{\partial}{\partial \mathbf{x}}\left[\frac{\partial L}{\partial \mathbf{x}'}\right] = 2\left(\hat{\mathbf{B}} - \lambda \mathbf{I_n}\right) \tag{B.11}$$

By using Eq. B.10 for several values of λ, the location of the optimum (either maximum or minimum) can be achieved. Choosing λ larger than the largest eigenvalue of $\hat{\mathbf{B}}$ will provide a maximum, whereas choosing it smaller than the smallest eigenvalue of $\hat{\mathbf{B}}$ will lead to a minimum [136]. The optimal value for the system response $\hat{y}(\mathbf{x})$ can be obtained by substituting $\mathbf{x}_s$ from Eq. B.10 into Eq. B.4.

B.2.2 Numerical Approach

As an alternative, the optimum response can be determined numerically using a simplex based direct search method developed by Nelder and Mead [137]. This numerical optimization method originally describes an iterative algorithm for the minimization of a function of n variables. A simplex is a convex hull in R^n, (n+1) vertices which do not lie in a hyperplane (Figure B.3).

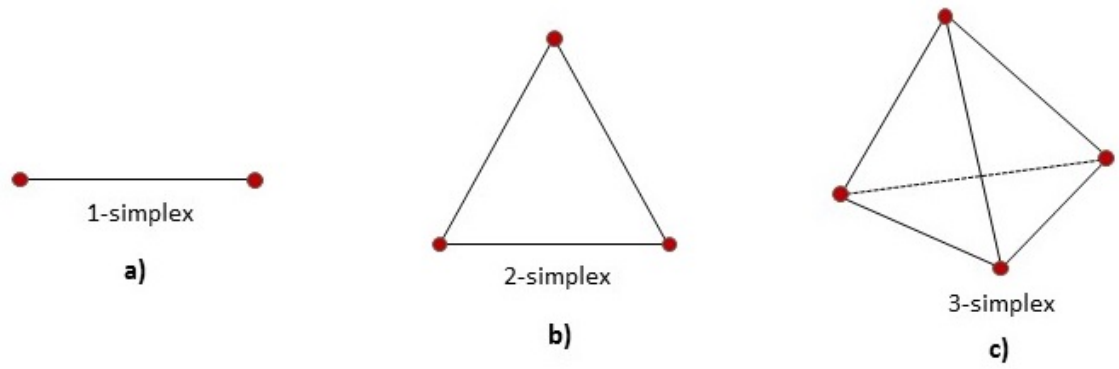


Figure B.3 Simplex types. **a)** A 1-simplex is a line, **b)** a 2-simplex is a triangle, and **c)** a 3-simplex is a tetrahedron.

The response function f is evaluated at all $n+1$ vertexes on the simplex. So we can sort the results and have $f(X_1) < f(X_2) < ... < f(X_n) < f(X_{n+1})$. The worst point X_w is then iteratively updated by reflection, expansion, 1-dimensional contraction or multiple contraction through the centroid of the remaining n points (X_g) so that the simplex adapts itself to the local topography and contracts while approaching towards the minimum [137]. The algorithm for the update of X_w to obtain the new vertex of the simplex is described below (Figure B.4) [138]:

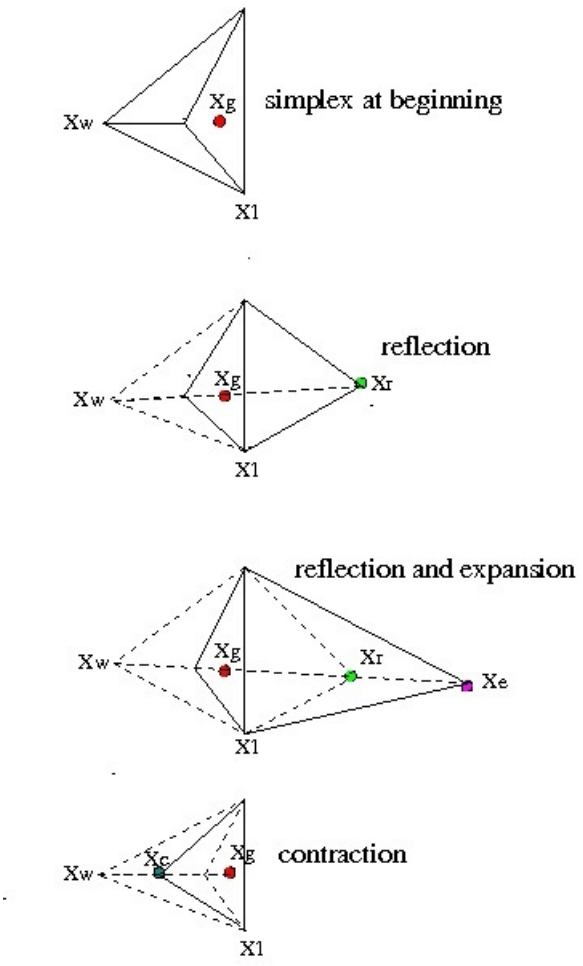


Figure B.4 Update of the simplex (tetrahedron) in 3-parameter optimization case [138].

1) Reflection: X_w is reflected through the centroid of the other n best points X_g to obtain the reflected point X_r.

2) Expansion: In case the response at the newly found reflected point X_r is better than the existing best point X_1, the simplex is expanded toward the newly found reflected point X_r.

3) Contraction: Whenever the observed response at the reflected point X_r is no longer more desirable than the existing best point X_1, then the simplex is contracted along 1-D through from the worst point X_w to the direction of X_g.

4) Multiple contraction: If the response at the newly reflected point X_r is found to be less desirable than the existing worst point X_w, the simplex will be contracted along all dimensions toward the existing best point X_1.

The crucial step of numerical optimization is the assignment of desirability functions developed by Derringer and Suich [54] to the responses. In this approach, each response is converted into a desirability function d_i over the interval [0,1]. The modeling of the desirabilities for the maximization and minimization cases are given as examples of modeling the desirabilities in Eq. B.12 and Eq. B.13, respectively. These are especially useful in case of multi-objective optimization since they allow balancing of all responses.

$$d_1 = \begin{cases} 0 & if\ y_{\mathrm{i}} \leq L_1 \\ \left[\frac{y_{\mathrm{i}} - L_1}{U_1 - L_1}\right]^{\omega_1} & if\ L_1 < y_{\mathrm{i}} < U_1 \\ 1 & if\ y_{\mathrm{i}} \geq U_1 \end{cases} \tag{B.12}$$

$$d_2 = \begin{cases} 1 & if\ y_{\mathrm{i}} \leq L_2 \\ \left[\frac{U_2 - y_{\mathrm{i}}}{U_2 - L_2}\right]^{\omega_2} & if\ L_2 < y_{\mathrm{i}} < U_2 \\ 0 & if\ y_{\mathrm{i}} \geq U_2 \end{cases} \tag{B.13}$$

For the optimization, ω_i's can be chosen according to the need of the experimenter depending on the goal. For instance, ω_i's greater than 1 more more emphasis to the goal, ω_i's less than 1 will do the opposite, since a small increase in the response above the lower limit will result in a decent desirability and ω_i's equal to 1 will give a ramp function for the desirability. Additionally, the desirability below the lower limit falls to 0 and above the high limit plateaus at 1 as shown (Figure B.5).

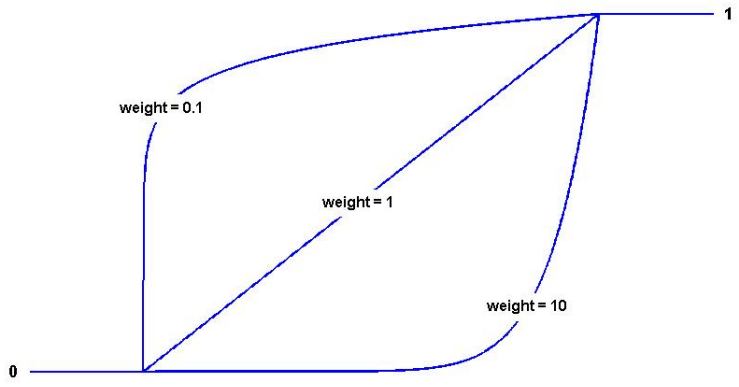


Figure B.5 Desirability functions according to weights for the maximization case.

In order to transform the multi-response problem into a single response problem, this individual desirability functions are converted into an overall desirability by taking their weighted geometric mean where each response assigned a relative importance factor r_i and this overall desirability, Eq. B.14 is maximized.

$$D = \left(\prod_{i}^{n} d_i^{r_i} \right)^{\frac{1}{\sum_i r_i}} \tag{B.14}$$

where n is the number of responses to be optimized.

B.2.3 Robust Optimization

If uncertainty or variability in the value of other factors is present, proper levels of controllable variables in a system are found using robust parameter design. In fact, these uncontrollable noise factors transmit variability to the process response. Therefore, the objective of robust parameter design is to obtain a system which is insensitive to unavoidable changes in the noise variables so that dispersion of the response has its smallest possible value [38] (Figure B.6). The robust solution is achieved by minimizing the propagation-of-error (PoE) of variables on the response of the system where PoE is defined as the standard deviation of the transmitted variability formulated generally as in Eq. B.15 involving taking partial derivatives of the regression model with respect to the individual factors.

$$POE = \sqrt{\sigma_y^2} = \sqrt{\sum_i \left(\frac{\partial y}{\partial x_i}\right) \sigma_{x_i}^2 + \sigma_{residual}^2} \tag{B.15}$$

where σ_y^2, σ_x^2 and $\sigma_{residual}^2$ represent the variance of the predicted response y, each input factor x_i and the unexplained residual error, respectively.

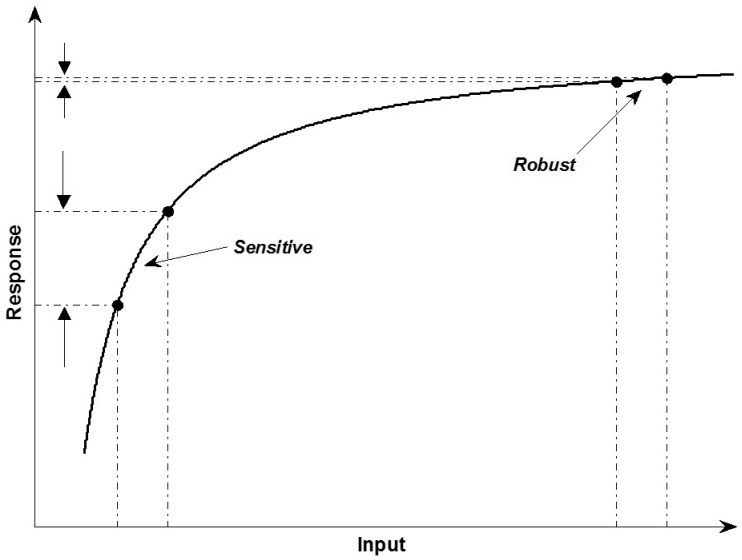


Figure B.6 The transmitted variation in the response vs. the choice of level of a control factor. The objective of the robust optimization is to minimize the transmitted variation to the response.

APPENDIX C. LIST OF PUBLICATIONS PRODUCED FROM THIS THESIS

1. Design and Evaluation of a Breast-Specific Collimator Using Response Surface Methodology and Monte Carlo Simulations, **D. Talat**, A. Guvenis, " *IEEE Transactions on Nuclear Science*, in press. DOI: 10.1109/TNS.2015.2484070

2. Meme Sintigrafisinde Torso Aktivitesinin Kolimatör Tasarımı Seçenekleri Üzerindeki Etkisi (Effect of Torso Activity on Collimator Design Options in Breast Scintigraphy), **D. Talat**, A. Guvenis, *BİYOMUT (National Conference on Biomedical Engineering)*, Istanbul, Turkey, Oct. 16-17, 2014.

3. Design and Evaluation of a Breast Specific Collimator Using Response Surface Methodology and Monte Carlo Simulations, **D. Talat**, A. Guvenis, *2013 Nuclear Science Symposium, Medical Imaging Conference and Workshop on Room-Temperature Semiconductor X-Ray and Gamma-Ray Detectors*, Seoul, Korea, Oct. 26 - Nov. 2, 2013.

4. 3B PET Tarayıcı Monte Carlo Benzetimleri: Geçerlilik Çalışması (Monte Carlo Simulations of A 3D PET Scanner: Validation Study), **D. Talat**, A. Guvenis, *BİYOMUT (National Conference on Biomedical Engineering)*, Istanbul, Turkey, Oct. 3-5, 2012.

5. Nükleer Tıp Monte Carlo Benzetimlerinin Küme Uygulaması: Geçerlilik Çalısması (Cluster Implementation of Nuclear Medicine Monte Carlo Simulations: Validation Study), **D. Talat**, A. Guvenis, *BİYOMUT (National Conference on Biomedical Engineering)*, Istanbul, Turkey, Oct. 13-16, 2011.

6. Cluster Application of Nuclear Medicine Monte Carlo Simulation Software on TR-Grid, **D. Talat**, A. Guvenis, *International Conference on Information Communication Technologies in Health*, Samos, Greece, July 14-16, 2011.

REFERENCES

1. Erdi, Y. E., "Limits of tumor detectability in nuclear medicine and PET," *Mol. Imaging Radionucl. Ther.*, Vol. 21, no. 1, pp. 23–28, 2012.

2. Pirotte, B., S. Goldman, J. M. Brucher, G. Zomosa, D. Baleriaux, J. Brotchi, and M. Levivier, "PET in stereotactic conditions increases the diagnostic yield of brain biopsy," *Stereotact. Funct. Neurosurg.*, Vol. 63, pp. 144–149, 1994.

3. Rose, A., "The sensitivity performance of the human eye on an absolute scale," *JOSA*, Vol. 38, no. 2, pp. 196–208, 1948.

4. MacDonald, L. R., R. L. Harrison, A. M. Alessio, W. C. J. Hunter, T. K. Lewellen, and P. E. Kinahan, "Effective count rates for PET scanners with reduced and extended axial field of view," *Phys. Med. Biol.*, Vol. 56, pp. 3629–3643, 2011.

5. von Schulthess, G. K., *Molecular Anatomic Imaging*, Philadelphia: Lippincott Williams & Wilkins, 2007.

6. Strother, S. C., M. E. Casey, and E. J. Hoffman, "Measuring PET scanner sensitivity: Relating countrates to image signal-to-noise ratios using noise equivalent counts," *IEEE Trans. Nucl. Sci.*, Vol. 37, pp. 783–788, 1990.

7. Box, G. E. P., and K. B. Wilson, "On the experimental attainment of optimum conditions (with discussion)," *Journal of the Royal Statistical Society Series B*, Vol. 13, no. 1, pp. 1–45, 1951.

8. Pani, R., R. Pellegrini, M. Betti, G. D. Vincentis, M. N. Cinti, P. Bennati, F. Vittorini, V. Casali, M. Mattioli, V. O. Cencelli, F. Navarria, D. Bollini, G. Moschini, G. Iurlaro, L. Montani, and F. de Notaristefani, "Clinical evaluation of pixellated NaI:Tl and continuous LaBr3:Ce, compact scintillation cameras for breast tumors imaging," *Nucl. Instr. & Meth. in Phys. Res. A*, Vol. 571, no. 1-2, pp. 475–479, 2007.

9. Fabbri, A., V. O. Cencelli, P. Bennati, M. N. Cinti, R. Pellegrini, G. D. Vincentis, and R. Pani, "Dual isotope imaging with labr3:ce crystal and H8500 PSPMT," *J. Inst.*, p. C02022, 2013.

10. Knoll, G. F., *Radiation Detection and Measurement*, New York: John Wiley & Sons, 2000.

11. Prekeges, J., *Nuclear Medicine Instrumentation*, Jones and Bartlett Publishers, LLC, 2011.

12. Cherry, S. R., and M. Dahlbom, "511 kev Photon Detectors," in *PET: Physics, Instrumentation, and Scanners* (Phelps, M. E., ed.), Springer Science+Business Media, LLC, 2006.

13. Hamilton, D., *Diagnostic Nuclear Medicine: A Physics Perspective*, Springer Verlag Berlin Heidelberg, 2004.

14. Bushberg, J. T., J. A. Seibert, E. M. Leidholdt, and J. M. Boone, *The Essential Physics of Medical Imaging*, Lippincott, Williams and Wilkins, 2012.

15. Khorshidi, A., M. Ashoor, S. H. Hosseini, and A. Rajaee, "Estimation of fan beam and parallel beam parameters in a wire mesh design," *J. Nucl. Med. Technol.*, Vol. 40, no. 1, pp. 37–43, 2012.

16. Fowler, A., "A molecular approach to breast imaging," *J. Nucl. Med*, Vol. 55, pp. 177–180, 2014.

17. Xu, H. B., L. Li, and Q. Xu, "Tc-99m sestamibi scintimammography for the diagnosis of breast cancer: meta-analysis and meta-regression," *Nucl. Med. Commun.*, Vol. 32, pp. 980–988, 2011.

18. Rhodes, D. J., C. B. Hruska, S. W. Phillips, D. H. Whaley, and M. K. O'Connor, "Dedicated dual-head gamma imaging for breast cancer screening in women with mammographically dense breasts," *Radiology*, Vol. 258, pp. 106–118, 2011.

19. Even-Sapir, E., "Scintimammography," in *Diseases of the Chest and Heart* (Hodler, J., G. K. von Schulthess, R. A. Kubik-Huch, and C. L. Zollikofer, eds.), pp. 247–249, Springer Milan, 2015.

20. Surti, S., "Radionuclide methods and instrumentation for breast cancer detection and diagnosis," *Semin. Nucl. Med.*, Vol. 43, pp. 271–280, 2013.

21. Majewski, S., D. Kieper, E. Curran, C. Keppel, B. Kross, A. Palumbo, V. Popov, A. G. Weisenberger, B. Welch, R. Wojcik, M. B. Williams, A. R. Goode, M. More, and G. Zhang, "Optimization of dedicated scintimammography procedure using detector prototypes and compressible phantoms," *IEEE Trans. Nucl. Sci.*, Vol. 48, no. 3, pp. 822–829, 2001.

22. Coover, L. R., G. Caravaglia, and P. Kuhn, "Scintimammography with dedicated breast camera detects and localizes occult carcinom," *J. Nucl. Med*, Vol. 45, pp. 553–558, 2004.

23. Mainiero, M. B., A. Lourenco, M. C. Mahoney, M. S. Newell, L. Bailey, L. D. Barke, C. D'Orsi, J. A. Harvey, M. K. Hayes, P. T. Huynh, P. M. Jokich, S. J. Lee, C. D. Lehman, D. A. Mankoff, J. A. Nepute, S. B. Patel, H. E. Reynolds, M. L. Sutherland, and B. G. Haffty, "ACR appropriateness criteria breast cancer screening," *J Am Coll Radiol.*, Vol. 10, pp. 11–14, 2013.

24. Weigert, J. M., M. L. Bertrand, L. Lanzkowsky, L. H. Stern, and D. A. Kieper, "Results of a multicenter patient registry to determine the clinical impact of breast-specific gamma imaging, a molecular breast imaging technique," *AJR Am J Roentgenol.*, Vol. 198, no. 1, pp. W69–W75, 2012.

25. Tadwalkar, R. V., J. A. Rapelyea, J. Torrente, L. R. Rechtman, C. B. Teal, A. P. Mcswain, C. Donnelly, A. B. Kidwell, C. M. Coffey, and R. F. Brem, "Breast-specific gamma imaging as an adjunct modality for the diagnosis of invasive breast cancer with correlation to tumour size and grade," *Br. J. Radiol.*, Vol. 85, pp. e212–e216, 2012.

26. Sun, Y., W. Wei, H.-W. Yang, and J.-L. Liu, "Clinical usefulness of breast-specific gamma imaging as an adjunct modality to mammography for diagnosis of breast cancer: a systemic review and meta-analysis," *Eur. J. Nucl. Med. Mol. Imaging*, Vol. 40, pp. 450–463, 2013.

27. Rhodes, D. J., C. B. Hruska, A. L. Conners, C. L. Tortorelli, R. W. Maxwell, K. N. Jones, A. Y. Toledano, and M. K. OConnor, "Molecular breast imaging at reduced radiation dose for supplemental screening in mammographically dense breasts," *AJR Am J Roentgenol.*, Vol. 204, no. 2, pp. 241–251, 2015.

28. Tornai, M. P., B. E. Patt, J. S. Iwanczyk, C. S. Levin, and E. J. Hoffman, "Discrete scintillator coupled mercuric iodide photodetector arrays for breast imaging," *IEEE Trans. Nucl. Sci.*, Vol. 44, no. 3, pp. 1127–1133, 1997.

29. Buvat, I., S. Laffont, J. L. Cloirec, P. Bourguet, and R. D. Paola, "Importance of the choice of the collimator for the detection of small lesions in scintimammography: a phantom study," *Phys. Med. Biol.*, Vol. 46, pp. 1343–1355, 2001.

30. Smith, M. ., S. Majewski, and A. G. Weisenberger, "Optimizing pinhole and parallel hole collimation for scintimammography with compact pixellated detectors," *IEEE Trans. Nucl. Sci.*, Vol. 50, pp. 321–326, June 2003.

31. Moré, M. J., P. J. Goodale, S. Majewski, and M. B. Williams, "Evaluation of gamma cameras for use in dedicated breast imaging," *IEEE Trans. Nucl. Sci.*, Vol. 53, no. 5, pp. 2675–2679, 2006.

32. Hruska, C. B., and M. K. O'Connor, "Effect of collimator selection on tumor detection for dedicated nuclear breast imaging systems," *IEEE Trans. Nucl. Sci.*, Vol. 53, no. 5, pp. 2680–2689, 2006.

33. Balta, S., and A. Guvenis, "Robust design of a breast scintigraphy collimator using Monte Carlo simulation and response surface method," in *European Journal of Nuclear Medicine and Molecular Imaging*, Vol. 34 (Suppl 2), p. 213, 2007.

34. Pani, R., R. Pellegrini, P. Bennati, M. N. Cinti, S. Ridolfi, R. Scafe, G. D. Vincentis, S. L. Meo, N. Lanconelli, F. Navarria, G. Moschini, A. Fabbri, E. D'Abramo, D. Sacco, V. O. Cencelli, and F. D. Notaristefani, "A novel parallel hole collimator for high resolution SPET imaging with a compact LaBr3 gamma camera," in *2008 IEEE NSS Conference Record*, pp. 3824–3828, 2008.

35. Weinmann, A. L., C. B. Hruska, and M. K. OConnor, "Design of optimal collimation for dedicated molecular breast imaging systems," *Med. Phys.*, Vol. 36, no. 3, pp. 845–856, 2009.

36. Robert, C., G. Montémont, V. Rebuffel, L. Verger, and I. Buvat, "Optimization of a parallel hole collimator/CdZnTe gamma-camera architecture for scintimammography," *Med. Phys*, Vol. 38, no. 4, pp. 1806–1819, 2011.

37. Kau, D., and S. D. Metzler, "Finding optimized conditions of slit-slat and multislit-slat collimation for breast imaging," *IEEE Trans. Nucl. Sci.*, Vol. 59, no. 1, pp. 62–69, 2012.

38. Myers, R., and D. C. Montgomery, *Response Surface Methodology - Process and Product Optimization using Designed Experiments*, New York: John Wiley & Sons, Inc., 2002.

39. Ljungberg, M., and S. E. Strand, "A Monte Carlo program for the simulation of scintillation camera characteristics," *Comput. Methods Programs Biomed*, Vol. 29, no. 4, pp. 257–272, 1989.

40. Wernick, M. N., and J. N. Aarsvold, eds., *Emission Tomography: The Fundamentals of PET and SPECT*, Elsevier, Inc., 2004.

41. Mann, S. D., K. L. Perez, E. K. E. McCracken, J. P. Shah, K. R. Choudhury, T. Z. Wong, and M. P. Tornai, "Quantification of Tc-99m sestamibi distribution in normal breast tissue using dedicated breast SPECT-CT," in *Breast Imaging* (Maidment, A. D. A., P. R. Bakic, and S. Gavenonis, eds.), pp. 402–409, Heidelberg, Germany: Springer-Verlag Berlin, 2012.

42. Goldsmith, S. J., W. Parsons, M. J. Guiberteau, L. H. Stern, L. Lanzkowsky, J. Weigert, T. F. Heston, E. Jones, J. Buscombe, and M. G. Stabin, "SNM practice guideline for breast scintigraphy with breast-specific γ-cameras 1.0," *J. Nucl. Med. Technol.*, Vol. 38, no. 4, pp. 219–224, 2010.

43. Bombardieri, E., C. Aktolun, R. P. Baum, A. Bishof-Delaloye, J. Buscombe, J. F. Chatal, L. Maffioli, R. Moncayo, L. Mortelmans, and S. N. Reske, "Breast scintigraphy: procedure guidelines for tumor imaging," *Eur J Nucl Med Mol Imaging*, Vol. 30, pp. BP107–BP114, 2003.

44. Maublant, J., M. de Latour, D. Mestas, A. Clemenson, S. Charrier, V. Feillel, G. L. Bouedec, P. Kaufmann, J. Dauplat, and A. Veyre, "Technetium-99m-sestamibi uptake in breast tumor and associated lymph nodes," *J. Nucl. Med.*, Vol. 37, no. 6, pp. 922–925, 1996.

45. Williams, M. B., M. J. More, D. Narayanan, S. Majewski, B. Welch, and D. A. Kieper, "Phantom study of radiotracer concentration quantification in breast scintigraphy," in *IEEE NSS/MIC Conference Record*, pp. 1882–1886, 2002.

46. Kieper, D., S. Majewski, B. Kross, V. Popov, A. G. Weisenberger, B. Welch, R. Wojcik, M. B. Williams, A. R. Goode, M. More, and G. Zhang, "Optimization of breast imaging procedure with dedicated compact gamma cameras," *Nucl. Instr. and Meth. in Phys. Res. A*, Vol. 497, pp. 168–173, 2003.

47. Ljungberg, M., *The SIMIND Monte Carlo Program Manual.*

48. Wagner, R. F., and D. G. Brown, "Unified SNR analysis of medical imaging systems," *Phys. Med. Biol.*, Vol. 30, pp. 489–518, 1985.

49. Loo, L. . N., K. Doi, and C. E. Metz, "A comparison of physical image quality indices and observer performance in the radiographic detection of nylon beads," *Phys. Med. Biol.*, Vol. 29, pp. 837–856, 1984.

50. Myers, K. J., H. H. Barrett, M. C. Borgstrom, D. D. Patton, and G. W. Seeley, "Effect of noise correlation on detectability of disk signals in medical imaging," *JOSA A*, Vol. 2, pp. 1752–1759, 1985.

51. Khuri, A., and S. Mukhopadhyay, "Response surface methodology," *Wiley Interdisciplinary Reviews: Computational Statistics*, Vol. 2, pp. 128–149, 2010.

52. "Design-Expert®, Stat-Ease, Inc., Minneapolis, MN, USA.."

53. Box, G. E. P., and D. W. Behnken, "Some new three-level designs for the study of quantitative variables," *Technometrics*, Vol. 2, pp. 455–475, 1960.

54. Derringer, G., and R. Suich, "Simultaneous optimization of several response variables," *J. Qual. Technol.*, Vol. 12, pp. 214–219, 1980.

55. Cherry, S. R., J. A. Sorenson, and M. E. Phelps, *Physics in Nuclear Medicine*, Pennsylvania: Elsevier Science, 2003.

56. Gunter, D. L., "Collimator design for nuclear medicine," in *Emission Tomography: The Fundamentals of PET and SPECT* (N.Wernick, M., and J. N. Aarsvold, eds.), pp. 153–168, San Diego, CA: Elsevier Academic Press, 2004.

57. Judy, P. F., R. G. Swensson, and M. Szulc, "Lesion detection and signaltonoise ratio in CT images," *Med. Phys.*, Vol. 8, pp. 13–23, 1981.

58. Muehllehner, G., and H. Luig, "Septal penetration in scintillation camera collimators," *Phys. Med. Biol.*, Vol. 18, pp. 855–862, 1973.

59. Cinti, M. N., R. Pani, F. Garibaldi, R. Pellegrini, M. Betti, N. Lanconelli, A. Riccardi, R. Campanini, G. Zavattini, G. D. Domenico, A. D. Guerra, N. Belcari, W. Bencivelli, A. Motta, A. Vaiano, and I. N. Weinberg, "Custom breast phantom for an accurate tumor SNR analysis," *IEEE Trans. Nucl. Sci.*, Vol. 51, no. 1, pp. 198–204, 2004.

60. Grüning, T., C. Brogsitter, I. W. Jones, and J. C. Heales, "Resolution recovery in planar bone scans: diagnostic value in metastatic disease," *Nucl. Med. Commun.*, Vol. 33, no. 12, pp. 1307–1310, 2012.

61. Raghunathan, P., P. J. Goodale, J. Klinger, M. Appleby, J. Atkinson, and M. B. Williams, "Matched collimators for pixellated gamma camera," in *2005 IEEE NSS Conference Record*, pp. 2001–2004, 2005.

62. Dickerscheid, D., J. Lavalaye, L. Romijn, and J. Habraken, "Contrast-noise-ratio (CNR) analysis and optimisation of breast-specific gamma imaging (BSGI) acquisition protocols," *EJNMMI*, Vol. 3, pp. 21–29, 2013.

63. Williams, M. B., D. Narayanan, M. J. Moré, P. J. Goodale, S. Majewski, and D. A. Kieper, "Analysis of position-dependent compton scatter in scintimammography with mild compression," *IEEE Trans. Nucl. Sci.*, Vol. 50, no. 5, pp. 1643–1649, 2003.

64. Yang, X., and H. Peng, "The use of noise equivalent count rate and the NEMA phantom for PET image quality evaluation," *Physica Medica*, 2015.

65. Kinahan, P. E., P. M. Cheng, A. M. Alessio, and T. K. Lewellen, "A quantitative approach to a weight-based scanning protocol for Pet oncology imaging," in *2005 IEEE NSS Conference Record*, pp. 1886–1890, 2005.

66. Badawi, R. D., and M. Dahlbom, "NEC: Some coincidences are more equivalent than others," *J. Nucl. Med.*, Vol. 46, no. 11, pp. 1767–1768, 2005.

67. MacDonald, L. R., R. E. Schmitz, A. M. Alessio, S. D. Wollenweber, C. W. Stearns, A. Ganin, R. L. Harrison, T. K. Lewellen, and P. E. Kinahan, "Measured count-rate performance of the discovery STE PET/CT scanner in 2D, 3D and partial collimation acquisition modes," *Phys. Med. Biol.*, Vol. 53, pp. 3723–3728, 2008.

68. Dhawan, V., K. Kazumata, W. Robeson, A. Belakhlef, C. Margouleff, T. Chaly, T. Nakamura, R. Dahl, D. Margouleff, and D. Eidelberg, "Quantitative brain PET. comparison of 2D and 3D acquisitions on the GE Advance scanner," *Clin. Pos. Imag.*, Vol. 1, pp. 135–144, 1998.

69. Komar, G., M. Teräs, M. Seppänen, J. Hirvonen, T. Vahlberg, J. Bergman, and H. Minn, "Comparison of 2D and 3D performance for FDG PET with different acquisition times in oncological patients," *Nucl. Med. Commun.*, Vol. 30, pp. 16–24, 2009.

70. Visvikis, D., D. Griffiths, D. C. Costa, J. Bomanji, and P. J. Ell, "Clinical evaluation of 2D versus 3D whole-body PET image quality using a dedicated BGO PET scanner," *Eur. J. Nucl. Med. Mol. Imaging*, Vol. 32, pp. 1050–1056, 2005.

71. Lodge, M. A., R. D. Badawi, R. Gilbert, P. E. Dibos, and B. R. Line, "Comparison of 2-dimensional and 3-dimensional acquisition for 18F-FDG PET oncology studies performed on an LSO-based scanner," *J. Nucl. Med.*, Vol. 47, pp. 23–31, 2006.

72. Thompson, C. J., "The effect of collimation on scatter fraction in multi-slice PET," *IEEE Trans. Nucl. Sci.*, 1988.

73. Valk, P. E., D. L. Bailey, D. W. Townsend, and M. N. Maisey, eds., *Positron Emission Tomography: Basic Science and Clinical Practice*, Springer Verlag London Berlin Heidelberg, 2004.

74. Badawi, R. D., P. K. Marsden, B. F. Cronin, J. L. Sutcliffe, and M. N. Maisey, "Optimization of noise-equivalent count rates in 3D PET," *Phys. Med. Biol.*, Vol. 41, pp. 1755–1776, 1996.

75. Lartizien, C., C. Comtat, P. E. Kinahan, N. Ferreira, B. Bendriem, and R. Trebossen, "Optimization of injected dose based on noise equivalent count rates for 2- and 3-dimensional whole-body PET," *J. Nucl. Med.*, Vol. 43, pp. 1268–1278, 2002.

76. Watson, C. C., M. E. Casey, B. Bendriem, J. P. Carney, D. W. Townsend, S. Eberl, S. Meikle, and F. P. Difilippo, "Optimizing injected dose in clinical PET by accurately modeling the counting-rate response functions specific to individual patient scans," *J. Nucl. Med.*, Vol. 46, pp. 1825–1834, 2005.

77. Danna, M., M. Lecchi, V. Bettinardi, M. C. Gilardi, C. W. Stearns, G. Lucignani, and F. Fazio, "Generation of the acquisition-specific NEC (AS-NEC) curves to optimize the injected dose in 3D 18F-FDG whole body PET studies," *IEEE Trans. Nucl. Sci.*, Vol. 53, pp. 86–92, 2006.

78. Walker, M. D., J. C. Matthews, M. C. Asselin, A. Saleem, C. Dickinson, N. Charnley, P. J. Julyan, P. M. Price, and T. Jones, "Optimization of the injected activity in dynamic 3D PET: A generalized approach using patient-specific NECs as demonstrated by a series of 15O-H2O scans," *J. Nucl. Med.*, Vol. 50, pp. 1409–1417, 2009.

79. Accorsi, R., J. S. Karp, and S. Surti, "Improved dose regimen in pediatric PET," *J. Nucl. Med.*, Vol. 51, pp. 293–300, 2010.

80. Kohlmyer, S. G., R. M. Miyaoka, and T. K. Lewellen, "Evaluation of low energy threshold settings for PVI PET systems," *IEEE Trans. Nucl. Sci.*, Vol. 46, pp. 2141–2145, 1999.

81. Yang, Y., Y.-C. Tai, S. Siegel, D. F. Newport, B. Bai, Q. Li, R. M. Leahy, and S. R. Cherry, "Optimization and performance evaluation of the microPET ii scanner for in vivo small-animal imaging," *Phys. Med. Biol.*, Vol. 49, pp. 2527–2545, 2004.

82. Turkington, T. G., J. W. Wilson, and J. G. Colsher, "Adjusting the low energy threshold for large bodies in PET," in *2004 IEEE NSS Conference Record*, pp. 2872–2876, 2004.

83. Mawlawi, O., J. W. Wilson, T. Pan, and T. G. Turkington, "Investigating the optimum lower energy threshold of a new research PET/CT scanner," in *2005 IEEE NSS Conference Record*, pp. 2054–2056, 2005.

84. Turkington, T. G., "Introduction to PET Instrumentation," *J. Nucl. Med. Technol.*, Vol. 29, no. 1, pp. 4–11, 2001.

85. Conti, M., "Tailoring PET time coincidence window using CT morphological information," *IEEE Trans. Nucl. Sci.*, Vol. 54, pp. 1599–1605, 2007.

86. Poon, J. K., M. L. Dahlbom, W. W. Moses, K. Balakrishnan, W. Wang, S. R. Cherry, and R. D. Badawi, "Optimal whole-body PET scanner configurations for different volumes of LSO scintillator: a simulation study," *Phys. Med. Biol.*, Vol. 57, pp. 4077–4094, 2012.

87. Schmidtlein, C. R., A. S. Kirov, S. A. Nehmeh, Y. E. Erdi, J. L. Humm, H. I. Amols, L. M. Bidaut, A. Ganin, C. W. Stearns, D. L. McDaniel, and K. A. Hamacher, "Validation of GATE Monte Carlo simulations of the GE Advance/Discovery LS PET scannersee," *Med. Phys.*, Vol. 33, pp. 198–208, 2006.

88. Jan, S., G. Santin, D. Strul, S. Staelens, Assié, D. Autret, S. Avner, R. Barbier, M. Bardiès, P. M. Bloomfield, D. Brasse, V. Breton, P. Bruyndonckx, I. Buvat, A. F. Chatziioannou, Y. Choi, Y. H. Chung, C. Comtat, L. F. D Donnarieix and, S. J. Glick, C. J. Groiselle, D. Guez, P.-F. Honore, S. Kerhoas-Cavata, A. S. Kirov, V. Kohli, M. Koole, M. Krieguer, D. J. van der Laan, F. Lamare, G. Largeron, C. Lartizien, D. Lazaro, M. C. Maas, L. Maigne, F. Mayet, F. Melot, C. Merheb, E. Pennacchio, J. Perez, U. Pietrzyk, F. R. Rannou, M. Rey, D. R. Schaart, C. R. Schmidtlein, L. Simon, T. Y. Song, J.-M. Vieira, D. Visvikis, R. V. de Walle, E. Wieërs, and C. Morel, "GATE: a simulation toolkit for PET and SPECT," *Phys. Med. Biol.*, Vol. 49, pp. 4543–4561, 2004.

89. Agostinelli, S., "Geant4-a simulation toolkit," *Nucl. Instrum. Methods Phys. Res. A*, Vol. 389, pp. 81–86, 2003.

90. "OpenGATE Collaboration." http://www.opengatecollaboration.org, 2004.

91. DeGrado, T. R., T. G. Turkington, J. J. Williams, C. W. Stearns, J. M. Hoffman, and R. E. Coleman, "Performance characteristics of a whole-body PET scanner," *J. Nucl. Med.*, Vol. 35, pp. 1398–1406, 1994.

92. Lewellen, T. K., S. G. Kohlmyer, R. S. Miyaoka, M. S. Kaplan, C. W. Stearns, and S. F. Schubert, "Investigation of the performance of the General Electric ADVANCE positron emission tomograph in 3D mode," *IEEE Trans. Nucl. Sci.*, Vol. 43, pp. 2199–2206, 1996.

93. Kirov, A. S., C. Danford, C. R. Schmidtlein, E. Yorke, J. L. Humm, and H. I. Amols, "PET quantification inaccuracy of non-uniform tracer distributions for radiation therapy," in *2007 IEEE NSS Conference Record*, pp. 2838–2841, 2007.

94. GE Medical Systems Technical Publications Direction 2103139-100 Revision 4, *Advance PET Imaging System Description And Specification*, 2002.

95. Brun, R., and F. Rademakers, "ROOT an object oriented data analysis framework," *Nucl. Instrum. Methods Phys. Res. A*, Vol. 389, pp. 81–86, 1997.

96. Staelens, S., J. D. Beenhouwer, D. Kruecker, L. Maigne, F. Rannou, L. Ferrer, Y. DAsseler, I. Buvat, and I. Lemahieu, "GATE: improving the computational efficiency," *Nucl. Instrum. Methods Phys. Res. A*, Vol. 569, pp. 341–345, 2006.

97. "TUBITAK ULAKBIM High Performance and Grid Computing Center." http://www.ulakbim.gov.tr/eng/ulaknet/trgrid/, 2007.

98. National Electrical Manufacturers Association, *NEMA Standards Publication NU-2 2007 Performance Measurements of Positron Emission Tomographs*, 2007.

99. Karakatsanis, N. A., G. Loudos, A. Rahmim, and K. S. Nikita, "Monte-Carlo based characterization of the counting rate (NECR) response for personalized optimization of the administered activity in clinical PET," *Front. Biomed. Technol.*, Vol. 1, pp. 14–34, 2014.

100. Peng, H., "Design study of a cardiac-dedicated PET system," *Nucl. Instr. & Meth. in Phys. Res. A*, Vol. 779, pp. 39–46, 2015.

101. Miyake, K. K., K. Matsumoto, M. Inoue, Y. Nakamoto, S. Kanao, T. Oishi, S. Kawase, K. Kitamura, Y. Yamakawa, A. Akazawa, T. Kobayashi, J. Ohi, , and K. Togashi, "Performance evaluation of a new dedicated breast PET scanner using NEMA NU4-2008 standards," *J. Nucl. Med.*, Vol. 55, pp. 1198–1203, 2014.

102. Cooper, R. J., *Performance of the SmartPET Positron Emission Tomography System for Small Animal Imaging*. PhD thesis, University of Liverpool, 2007.

103. Yamada, R., M. Watanabe, T. Omura, N. Sato, K. Shimizu, M. Takahashi, K. Ote, A. Katabe, T. Moriya, K. Sakai, T. Yamashita, and E. Tanaka, "Development of a small animal PET scanner using DOI detectors," *IEEE Trans. Nucl. Sci.*, Vol. 55, no. 3, pp. 906–911, 2008.

104. Wang, Y., J. Seidel, B. M. W. Tsui, J. J. Vaquero, and M. G. Pomper, "Performance evaluation of the GE Healthcare eXplore VISTA dual-ring small-animal PET scanner," *J. Nucl. Med*, Vol. 47, no. 11, pp. 1891–1900, 2006.

105. Laurence, T. L., and J. A. Kolthammer, "PET calibrations with varying coincidence windows." US Patent 8,987,659, 2015.

106. Wang, W., and X. Niu, "Random coincidence reduction in positron emission tomography using tangential time-of-flight mask." US Patent App. 13/472,533, 2013.

107. Schug, D., J. Wehner, P. M. Dueppenbecker, B. Weissler, P. Gebhardt, B. Goldschmidt, A. Salomon, F. Kiessling, and V. Schulz, "PET performance and MRI compatibility evaluation of a digital, ToF-capable PET/MRI insert equipped with clinical scintillators," *Med. Phys. Biol.*, Vol. 60, pp. 7045–7067, 2015.

108. Freedenberg, M. I., R. D. Badawi, A. F. Tarantal, and S. R. Cherry, "Performance and limitations of positron emission tomography (PET) scanners for imaging very low activity sources," *Physica Medica*, Vol. 30, pp. 104–110, 2014.

109. Efthimiou, N., G. Loudos, N. A. Karakatsanis, and G. S. Panayiotakis, "Effect of 176lu intrinsic radioactivity on dual head PET system imaging and data acquisition, simulation, and experimental measurements," *Med. Phys.*, Vol. 40, no. 11, 2013.

110. Cook, G. J. R., "Oncological molecular imaging: nuclear medicine techniques," *The British Journal of Radiology*, Vol. 76 (Suppl 2), pp. S152–S158, 2003.

111. Haynor, D. R., R. L. Harrison, and T. K. Lewellen, "The use of importance sampling techniques to improve the efficiency of photon tracking in emission tomography simulations," *Med. Phys*, Vol. 18, no. 5, pp. 990–1001, 1991.

112. Ljungberg, M., *Monte Carlo Calculations in Nuclear Medicine: Applications in Diagnostic Imaging*, Bristol: IOP Publishing, 1998.

113. Buvat, I., and I. Castiglioni, "Monte Carlo simulations in SPET and PET," *Q. J. Nucl. Med.*, Vol. 46, no. 1, pp. 48–61, 2002.

114. Zaidi, H., ed., *Quantitative Analysis in Nuclear Medicine Imaging*, Springer Science+Business Media, Inc., 2006.

115. Nelson, W. R., H. Hirayama, and D. W. O. Rogers, "The EGS4 code system," tech. rep., Stanford Linear Accelerator Center, 1985.

116. Forster, R. A., and T. N. K. Godfrey, "MNCP - a General Monte-Carlo code for neutron and photon transport," *Lecture Notes in Physics*, Vol. 240, pp. 33–35, 1985.

117. Halbleib, J. A., R. P. Kensek, T. A. Mehlhorn, G. D. Valdez, S. M. Seltzer, and M. J. Berger, "ITS version 3.0: the integrated TIGER series of coupled electron/photon Monte Carlo transport codes," tech. rep., Sandia National Laboratories, 1992.

118. Thompson, C. J., J. Morenocantu, and Y. Picard, "PETSIM - Monte-Carlo simulation of all sensitivity and resolution parameters of cylindrical positron imaging-systems," *Phys. Med. Biol*, Vol. 37, no. 3, pp. 731–749, 1992.

119. Reilhac, A., C. Lartizien, N. Costes, S. Sans, C. Comtat, R. N. Gunn, and A. C. Evans, "PET-SORTEO: A Monte Carlo-based simulator with high count rate capabilities," *IEEE Trans. Nucl. Sci.*, Vol. 51, no. 1, pp. 46–52, 2004.

120. Lewellen, T., "The SimSET program," in *Monte Carlo Calculation in Nuclear Medicine: Applications in Diagnostic Imaging* (Ljungberg, M., ed.), pp. 77–92, Bristol: IOP Publishing, 1998.

121. Kimiaei, S., M. Ljungberg, and S. A. Larsson, "Evaluation of optimally designed planar-concave collimators in single-photon emission tomography," *Eur. J. Nucl. Med.*, Vol. 24, no. 11, pp. 1398–1404, 1997.

122. Carrier, J. F., L. Archambault, and L. Beaulieu, "Validation of GEANT4 and an object-oriented Monte Carlo toolkit and for simulations in medical physics," *Med. Phys*, Vol. 31, no. 3, pp. 484–492, 2004.

123. Poon, E., and F. Verhaegen, "Accuracy of the photon and electron physics in GEANT4 for radiotherapy applications," *Med. Phys*, Vol. 32, no. 6, pp. 1696–1711, 2005.

124. Jarlskog, C. Z., and H. Paganetti, "Physics settings for using the geant4 toolkit in proton therapy," *IEEE Trans. Nucl. Sci.*, Vol. 55, no. 3, pp. 1018–1025, 2008.

125. Lechner, A., V. N. Ivanchenko, and J. Knobloch, "Validation of recent geant4 physics models for application in carbon ion therapy," *Nucl. Instr. & Meth. in Phys. Res. B*, Vol. 268, pp. 2343–2354, 2010.

126. Jan, S., D. Benoit, E. Becheva, T. Carlier, F. Cassol, P. Descourt, T. Frisson, L. Grevillot, L. Guigues, L. Maigne, C. Morel, Y. Perrot, N. Rehfeld, D. Sarrut, D. R. Schaart, S. Stute, U. Pietrzyk, D. Visvikis, N. Zahra, and I. Buvat, "GATE V6: a major enhancement of the GATE simulation platform enabling modelling of CT and radiotherapy," *Phys. Med. Biol.*, Vol. 56, no. 4, pp. 881–901, 2011.

127. Beenhouwer, J. D., S. Staelens, D. Kruecker, L. Ferrer, Y. D'Asseler, I. Lemahieu, and F. R. Rannou, "Cluster computing software for GATE simulations," *Med. Phys*, Vol. 34, no. 6, pp. 1926–1933, 2007.

128. Beenhouwer, J. D., D. A. Kruecker, S. G. Staelens, L. Ferrer, A. F. Chatziioannou, and F. R. Rannou, "Distributed computing platform for PET and SPECT simulations with GATE," in *2005 IEEE NSS Conference Record*, pp. 2437–2440, 2005.

129. Venter, G., R. T. Haftka, and J. J H Starnes, "Construction of response surfaces for design optimization applications," in *AIAA, NASA, and ISSMO, Symposium on Multidisciplinary Analysis and Optimization*, pp. 548–564, 1996.

130. Carley, K. M., N. Y. Kamneva, and J. Reminga, "Response surface methodology," tech. rep., Carnegie Mellon University, Center for Computational Analysis of Social and Organizational Systems, 2004.

131. Montgomery, D. C., *Design and Analysis of Experiments*, New York: John Wiley & Sons, 2005.

132. Plackett, R. L., and J. P. Burman, "The design of optimum multifactorial experiments," *Biometrika*, Vol. 33, pp. 305–325, 1946.

133. Box, G. E. P., "Multi-factor designs of first order," *Biometrika*, Vol. 39, pp. 49–57, 1952.

134. Khuri, A. I., and J. A. Cornell, *Response Surfaces*, New York: Dekker, 1996.

135. Hoerl, A. E., "Optimum solutions of many variable equations," *Chem. Eng. Prog.*, Vol. 55, pp. 69–78, 1959.

136. Draper, N. R., "Ridge analysis of response surfaces," *Technometrics*, Vol. 5, pp. 469–479, 1963.

137. Nelder, J. A., and R. Mead, "A simplex method for function minimization," *Comp. J.*, Vol. 7, no. 4, pp. 308–313, 1965.

138. Jia, B. http://www.codeguru.com/cpp/article.php/c17505/Simplex-Optimization-Algorithm-and-Implemetation-in-C-Programming.htm.